The manuscript *"Monogenetic volcanoes as windows into transcrustal mush: A case study of Slamet and Loyang volcanoes, Central Java"* is under review at the Journal of Volcanology and Geothermal Research. This version (08/25/2023) is the same as our initial submission on June 15th, 2023. Initial reviewer reports have been completed, and this manuscript is currently being modified by the corresponding author according to the editor's instructions. Re-submission of the manuscript is planned by September 15th, 2023.

Monogenetic volcanoes as windows into transcrustal mush: A case study of Slamet and Loyang volcanoes, Central Java

Nicholas D. Barber[1,2,3*], Sophie L. Baldwin[1,4], Marie Edmonds[1],
Felix O. Boschetty[5], Haryo Edi Wibowo[6], and Agung Harijoko[6]

[1]Department of Earth Sciences, University of Cambridge, UK
[2]Department of Earth and Planetary Science, McGill University, Montreal, Canada
[3]Department of Earth and Environmental Geoscience, Washington and Lee University, Virginia, USA
[4]School of Geosciences, University of Edinburgh, UK
[5]Institute of Geophysics and Tectonics, School of Earth and Environment, University of Leeds, Leeds, UK
[6]Departemen Teknik Geologi, Universitas Gadjah Mada, Yogyakarta, Indonesia

June 19th, 2023

Abstract

Monogenetic volcanic "fields (MVFs) are commonly associated with long-lived polygenetic composite volcanoes in many tectonic settings. The association between polygenetic and monogenetic volcanoes has raised questions as to the source of monogenetic melts – specifically, whether they are derived from the transcrustal mush underlying a nearby polygenetic volcano, or from a different batch of parental magma. To address this question, we studied a well-constrained suite of scoria samples from Gunung Slamet in Central Java, Indonesia, and its most distal monogenetic scoria cone, Gunung Loyang. Slamet is composed of calc-alkaline basalts, and has an extensive MVF on its eastern flank, similar to other Indonesian volcanoes. We analyzed the textural and chemical features of the olivine cargo in both volcanoes, including olivine- and clinopyroxene-hosted melt inclusions. These melt inclusions are the first such analyzed for volatile element contents (H_2O, CO_2) in the Slamet-Loyang system. We applied hierarchical clustering and mass balance models to constrain the features of the olivine populations in both systems. The olivines in both volcanoes cluster in five distinct textural groups, defined by the presence or lack of zoning and resorption, and according to the type and degree of zoning they exhibit. Olivines show a range of moderate to evolved Fo%, and they also show significant variation in nickel contents (50-1600 ppm). By estimating saturation pressures of entrapped melt inclusions, we observe that Loyang olivines are drawn from a similar petrological system as Slamet, but from a deeper (12 km.) and more mafic source. Our work suggests that monogenetic volcanoes like Loyang can be used as “petrological windows” into the deeper crustal levels of mush at composite stratovolcanoes and their associated MVFs.

1 Introduction

Small-scale, spatially diffuse volcanism is one of the most prevalent igneous processes operating on the surface of both the Earth (Németh and Kereszturi 2015; Cañon-Tapia 2016; Walker 1993; Wood 1980) and other planetary bodies (Ivanov and Head 2013; Brož and Hauber 2012). Monogenetic volcanoes (also called flank, scoria, pyroclastic, or parasitic cones; see relevant reviews for disambiguation autocitenemeth2015monogenetic, smith2017source) are usually defined as having short eruptive lifespans (active over the course of a single eruption usually) with limited material output and simpler magmatic plumbing systems compared to their "polygenetic," or longer-lived and larger volcanic counterparts. For more details on the defining characteristics of monogenetic volcanism, see comprehensive reviews (Gábor Kereszturi and Németh 2012; Németh and Kereszturi 2015; Cañon-Tapia 2016; I. Smith and Németh 2017). However, under the right circumstances, monogenetic volcanoes can produce a comparable material output (total volumetric output across dozens or hundreds of centres within a defined region, called a monogenetic volcanic field or MVF) to a polygenetic volcano, yet with generally shorter lifespans; sometimes persisting centuries or millenia (Cañon-Tapia 2016; Gábor Kereszturi and Németh 2012; Németh and Kereszturi 2015).

Monogenetic volcanoes are common in both intraplate (Gencalioglu-Kuscu 2011; Jankovics, Harangi, et al. 2015; Cañon-Tapia 2016; McGee et al. 2013; I. E. Smith, Brenna, and Cronin 2021; Boyce et al. 2015) and subduction zone (Walowski et al. 2019; Carn and Pyle 2001; Cañon-Tapia 2016; Larrea et al. 2021; Romero et al. 2022) settings. One subduction zone locality littered with monogenetic volcanism is Java, Indonesia (Cañon-Tapia 2016), where polygenetic volcanoes show strong associations with monogenetic vents (Carn and Pyle 2001; Harijoko, Noor, et al. 2018; Marliyani et al. 2020). Polygenetic volcanoes like Lamongan, Slamet, Tengger-Bromo, Ijen, Arjuno-Welirang, Penanggungan, the Dieng plateau, Karang, and Tangkuban Perahu have parasitic vents like scoria cones, tuff rings, and maars on many of their flanks. This monogenetic activity is often expressed relative to the orientation of the direction of maximum horizontal stress (Marliyani et al. 2020) which changes along-arc as a function of crustal stress field changes (Marliyani et al. 2020). These preferential alignments of monogenetic volcanoes in Java are believed to reflect the emplacement of dikes in response to a changing crustal stress field (Marliyani et al. 2020). Such common MVF-polygenetic associations may also be related to the changing compressional-extensional stress regimes associated with the counter-clockwise rotation of Java over the past 20 Mya (Widiyantoro and Hilst 1997).

Arc-related monogenetic volcanoes present a challenge for volcanic hazard assessment, as the signals leading up to their eruptions are typically poorly monitored and understood (Walowski et al. 2019; Johnson and Cashman 2020). Of importance to mitigating the risk posed by these systems is an understanding of their plumbing systems, which have been shown to have a similar degree of geochemical and textural complexity to polygenetic centres (Walowski et al. 2019; Larrea et al. 2021; McGee et al. 2013; Straub et al. 2008; Carn and Pyle 2001; Coote and Shane 2018; Coote, Shane, and Fu 2019; Johnson and Cashman 2020). For example, the degree to which the magmatic storage systems of monogenetic volcanoes are connected to those of their spatially-associated larger polygenetic volcanoes is unclear (Németh and Kereszturi 2015; Cashman, Sparks, and Blundy 2017; Valentine and Gregg 2008).

Monogenetic scoria cones may either (1) tap the upper crustal (< 15 km.) reservoirs that feed a larger, long-lived polygenetic complex (Rawson et al. 2016; Walowski et al. 2019), or (2) directly tap a mantle-sourced magma at deeper levels in the crust, bypassing any shallow reservoir (Németh and Kereszturi 2015; Cañon-Tapia 2016; I. Smith and Németh 2017). In some cases, erupted products from scoria cones show a general increase in MgO and decrease in SiO_2 contents associated with cones increasingly further from their polygenetic centre (Rawson et al. 2016). This variability has been ascribed to mixtures of crustal and mantle-sourced melts (Straub et al. 2008), with more mafic, mantle-derived melts dominating monogenetic volcanism the further away from a polygenetic volcano (Rawson et al. 2016). Individual MVFs display a great degree of variability in the storage depths of magma prior to eruption, and in the source processes driving their eruptions (McGee et al. 2013; Coote, Shane, and Fu 2019; Coote and Shane 2018; Walowski et al. 2019). Both theoretical (Gábor Kereszturi and Németh 2012; Cañon-Tapia 2016; I. Smith and Németh 2017) and observational (Rawson et al. 2016; Walowski et al. 2019; Coote and Shane 2018; Coote, Shane, and Fu 2019) studies have discussed the polygenetic-monogenetic connection, with recent literature reviews emphasizing that this apparent binary system (monogenetic versus polygenetic) is much more likely a spectrum of volcano types, based on tectonic, geological, and magmatic variables (I. Smith and Németh 2017; Cañon-Tapia 2016). However, these studies raise an important question: to what extent are monogenetic volcanoes and their plumbing systems independent, or distinct, from their polygenetic centre (Cañon-Tapia 2016)? This question of connectedness likely depends on what depth below a volcano one is interested in (Cañon-Tapia 2016). Careful attention has been paid to the mantle source of mafic MVFs (Rawson et al. 2016; McGee et al. 2013; Straub et al. 2008; Carn and Pyle 2001), where mineral chemistry systematics, whole rock chemistry. Isotopic evidence has been used to reconstruct mantle-source processes in monogenetic volcanoes e.g., reactive melt channel flow (Rawson et al. 2016) or mantle lithologies like hybrid pyroxenite-peridotite sources (Straub et al. 2008). These studies have emphasized how some monogenetic systems are considered "closed," and do not preserve much evidence of crustal interaction (Coote, Shane, and Fu 2019).

Other work has shown how open system processes can occur at monogenetic volcanoes, with or without the involvement of other magmatic systems. These open-system interactions have been observed in systems like Cinder Cone, USA, where melt inclusion chemistry points to significant crustal contributions by granitic batholiths (Walowski et al. 2019), or in the Kaikohe-Bay of Islands volcanic field, NZ (Coote and Shane 2018; Coote, Shane, and Fu 2019) where interactions between crystalline mushes and monogenetic source magmas has been demonstrated using clinopyroxene phenocryst chemistry and thermobarometry (Coote and Shane 2018). A recent study of Cerro Negro pyroclastic cone (northern Chile), which is nested within Tálar caldera in the Andes, provides stratigraphic and whole rock chemistry evidence of polybaric fractionation and magma mixing within a simple monogenetic plumbing system (Romero et al. 2022), indicating that even independent of a neighboring polygenetic plumbing system, monogenetic volcanoes can develop complex magma feeder systems. Furthermore, hybrid open and closed-system processes have been identified in MVFs both in Europe (Bakony-Balaton Highland VF) (Jankovics, Sági, et al. 2019) and North America (Big Pine volcanic field) (Gao, Lassiter, and Ramirez 2017), based on evidence from olivine mineral chemistry (Jankovics, Sági, et al. 2019; Coote, Shane, and Fu 2019) and whole rock trace and isotopic geochemistry (Gao, Lassiter, and Ramirez 2017; Coote, Shane, and Fu 2019). In both cases primitive mantle and mineral compositions are preserved alongside more evolved crustal material (Jankovics, Sági, et al. 2019; Gao, Lassiter, and Ramirez 2017) in eruptive successions at individual scoria cones. Some flank scoria cones, like the Okahune craters (Houghton and Hackett 1984) and Hauhungatahi scoria cone (Cameron et al. 2010) on the slopes of Ruapehu volcano, New Zealand, have been shown to exhibit open-system processes connected to the emergence of Ruapehu's polygenetic edifice (Hackett and Houghton 1989; Houghton and Hackett 1984; Cameron et al. 2010). Despite both Okahune and Hauhungatahi erupted material having significantly more mafic compositions (two-pyroxene, olivine andesite) than Ruapehu (Houghton and Hackett 1984; Cameron et al. 2010), Okahune and Hauhungatahi both show structural relationships (the N-NE trending lineament associated with the Taupo caldera) (Hackett and Houghton 1989) that suggest they share a common magmatic source to the more evolved (plagioclase-dominated) andesitic eruptive products at Ruapehu (Hackett and Houghton 1989; Houghton and Hackett 1984). Ar/Ar dates show that Hauhungatahi's erutive activity ceased hundreds of Ka prior to Ruapehu's activity (Cameron et al. 2010). Furthermore, despite some evidence of earlier contamination, radiogenic isotopes show that Hauhungatahi magmas experienced less crustal interaction than Ruapehu magmas (Cameron et al. 2010). Thus, Ruapehu appears to be an example of an andesitic polygenetic edifice which emerged after earlier, basaltic monogenetic volcanism (Cameron et al. 2010). These earlier basaltic magmas were, in Hauhungatahi's case, modified by the crust to a minor degree, but did not reach the levels of shallow differentiation and crustal interaction reached by andesitic Ruapehu magmas (Cameron et al. 2010).

These examples in New Zealand, North America, Europe, and the Andes illustrate that monogenetic volcanoes are capable of supporting complex plumbing systems and exhibiting open-system behaviors, sometimes independent of or associated with polygenetic volcanic centres. However, there is little emphasis in the literature on temporally coincident monogenetic/polygenetic volcanism, and whether monogenetic volcanoes erupting around the same time as their polygenetic neighbors might interact with or even share a magma plumbing system. Both Cerro Negro (N. Chile) (Romero et al. 2022) and Hauhungatahi (Cameron et al. 2010) preceded major polygenetic activity, and therefore might have plumbing system independent of the one currently feeding eruptions at Ruapehu. Understanding such "hybrid" polygenetic-monogenetic systems is crucial systematic understanding of the eruptive products and magma source regions feeding different eruption styles. Slamet volcano in Central Java shows such hybrid behavior, with predominantly Strombolian eruptive styles at Slamet itself, and pyroclastic to phreatomagmatic eruptions among its 30 flank scoria cones. While we know that Slamet's whole rock compositions and crystal populations have changed through time at these eruptive centers (Harijoko, Noor, et al. 2018; Agung Harijoko et al. 2021), there has yet been no attempt to link these changes in magma compositions to different kinds of source magmas. Furthermore, it is not known whether the Strombolian activity at Slamet, and the short-lived hydromagamatic eruptions of scoria cones like Gunung (Indonesian synonym of the English "Mount") Loyang, were fed by discrete, shallow, and volatile-poor melts sourced from depth, or whether they represent the products of a complex transcrustal mush. These end-member magmatic architecture scenarios would provide divergent estimates of the kinds of future eruptions we can expect from either Slamet or its scoria cones. More pressingly, recent work has demonstrated Slamet, while known historically for low-energy Strombolian eruptions, has been capable in the past of at least seven pyroclastic eruptions over the Holocene epoch (Agung Harijoko et al. 2021). In order to understand what magmatic processes drive eruptions and trigger their recurrence within hybrid systems like Slamet and Loyang, there is an urgent need for a full petrological understanding of these systems.

In this manuscript, we investigate the eruptive products of Gunung Slamet, a long-lived basaltic stratovolcano in Central Java, and Gunung Loyang, Slamet's most distal scoria cone. Our goal in this manuscript is to determine (1) where each volcanoes magma is drawn from in the crust and (2) whether the magma storage systems beneath these volcanoes are linked via common crustal reservoirs. Prior study of Slamet revealed that magma mixing coupled with fractional crystallization explains the diverse range of mineralogical populations contained within the volcanoes' erupted basalts (Reubi, I. A. Nicholls, and Kamenetsky 2003). However, this earlier work was not able to establish where in the crust these melts are stored, or the volatile budget underpinning this explosive system. Furthermore, we do not know how Slamet's MVF fits into its volcanic history - might scoria cones like Loyang draw on the parental magma reservoir of Slamet? Or are these scoria cones fed by a distinct magma source? With these knowledge gaps in mind, we report major, minor, volatile, and trace element compositions of whole rock, major mineral phases, glass, and melt inclusions (MIs) sourced from the scoriaceous material gathered from Slamet and Loyang on field campaigns in 2017-2018 (Harijoko, Gunawan, et al. 2018; Harijoko, Noor, et al. 2018; Agung Harijoko et al. 2021). The MIs measured in this study are the first such measured in the Slamet system: their inclusions represents an important effort to fill a gap in our understanding of Java's along-arc magma storage conditions in the Eastern portion of the Sunda Arc (Vigouroux et al. 2012). We hope this work will motivate further study of hybrid polygenetic-monogenetic magma storage in Southeast Asia.

2 Geological Setting

Gunung Slamet is basaltic-andesitic stratovolcano located in Central Java (see Figure 1). With a summit elevation of 3,428 m.a.s.l., Slamet is the second tallest volcano in Java, second only to Semeru, and is occupied south of its main edifice by a moderate-sized city, Purwokerto, which has a population of over 200,000. Slamet is typical of basaltic volcanism in the Sunda Arc, which is one of the most active subduction zones on Earth(Venzke 2013; Wheller et al. 1987). Geologically, Slamet has been subdivided between Tua (or "Old") and Muda (or "Young") Slamet formations, hereafter referred to as TS and MS, on the west and east slopes of the edifice respectively(Vukadinovic and Igan Sutawidjaja 1995; Vukadinovic and I. Nicholls 1989; Sutawidjaja, Aswin, and Sitorus 1985). These categorizations were made on the basis of structural, morphological, and geochemical differences between the two flanks of the volcano, where TS has been recognized as an eroded earlier edifice, and MS as corresponding to the modern eruptive area(Sutawidjaja, Aswin, and Sitorus 1985; Vukadinovic and I. Nicholls 1989). TS products are more intermediate in composition than the more mafic MS volcanic products(Vukadinovic and I. Nicholls 1989; Vukadinovic and Igan Sutawidjaja 1995; Reubi, I. A. Nicholls, and Kamenetsky 2003; Harijoko, Milla, et al. 2020; Agung Harijoko et al. 2021). Some authors have argued that both units share a similar mantle source while having distinct evolutionary histories(Harijoko, Milla, et al. 2020; Reubi, I. A. Nicholls, and Kamenetsky 2003) based on their trace element, rare earth element (REE), and radiogenic isotope contents. In general, Slamet is one of Java's more spectacular examples of Strombolian-style volcanism (see Figure 2), with considerable petrographic and mineralogical evidence of magma mingling in the deep crust(Reubi, I. A. Nicholls, and Kamenetsky 2003; Vukadinovic and Igan Sutawidjaja 1995). Prior mineral analyses(Reubi, I. A. Nicholls, and Kamenetsky 2003) and whole rock geochemistry(Vukadinovic and Igan Sutawidjaja 1995; Vukadinovic and I. Nicholls 1989) work has focused on both the crustal processes and mantle sources of magmas at this polygenetic volcano. Prior work on the mineral chemistry of Slamet basalts has indicated that open system processes dominated by varying degrees of harzburgite and lherzolite melting, coupled with extensive melt-mixing within an existing magma mush, define MS eruptions (Reubi, I. A. Nicholls, and Kamenetsky 2003). Meanwhile, whole rock chemistry analysis has shown that TS magma mushes were influenced by the fractionation of amphibole, and only later evolved to a more mafic, water poor composition (Vukadinovic and Igan Sutawidjaja 1995) seen in MS basalts.

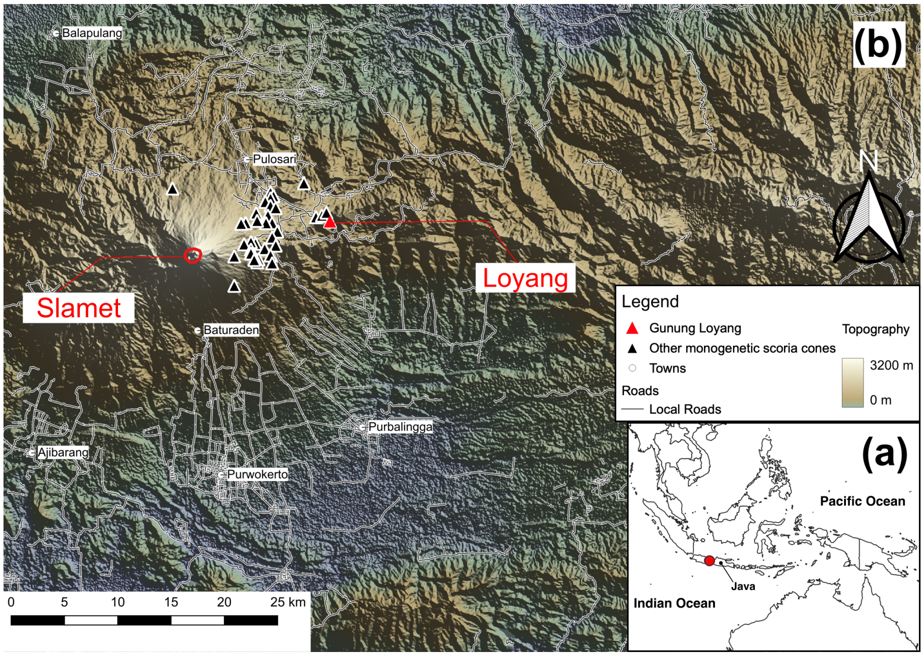

Figure 1: a) inset map showing geographic location of Slamet volcano (red circle) within the borders of Indonesia b)Regional map showing location of Slamet's crater (red circle) Mt. Loyang (red triangle), and other monogenetic scoria cones (black triangles). Major population centres and roads overlain. Map colored to show elevayion in m.a.s.l. using Scientific Color Map (Crameri 2019). Map made in QGIS 3.22.

Slamet is also one of Indonesia's most active volcanoes (Philibosian and Simons 2011), with tens of eruptions throughout the 20th century (Figure 2) and a recent eruption in 2014 (Venzke 2013). Slamet has had documented historical eruptions as far back as 1772 C.E., where the scale of the eruptions has not exceeded VEI 2 in available records (Venzke 2013). As shown in Figure 2, Slamet has produced frequent, small Strombolian eruptions at relatively regular time intervals over the past 200+ years. The lack of any eruptions with a VEI ≥ 2 in the past few centuries represents a remarkable consistency in Slamet's eruptive pattern, which contrasts with the deeper-time geological record. While older deposits are not dated, they show that Slamet is capable of producing VEI > 2 eruptions dominated by pyroclastic density currents and flank collapse deposits reminiscent of the 1980 eruption of Mt. St. Helens (VEI ≥ 4) (Agung Harijoko et al. 2021). Slamet's E and NE flanks are defined by a different kind of eruptive activity: diffuse scoria cones making up an extensive MVF. This MVF has been developed on top of MS material (Igan S Sutawidjaja and Sukhyar 2009). Of these scoria cones, Loyang (see Figure 1) is among the most distal, located 14 km. E of Slamet's summit. Loyang's deposits have well-constrained stratigraphy (Igan S Sutawidjaja and Sukhyar 2009), and the scoria cone shows evidence of a complex eruptive history (Harijoko, Gunawan, et al. 2018) defined by varying degrees of phreatomagmatic and Strombolian-style eruptive deposits. This eruptive pattern mirrors those seen in other basaltic monogenetic volcanoes (Németh and Kereszturi 2015; Larrea et al. 2021; Jankovics, Harangi, et al. 2015). Loyang has exhibited repeated Vulcanian and Strombolian style eruptions, with a much stronger influence of external water producing phreatomagmatic eruptions later in the scoria cone's history (Harijoko, Gunawan, et al. 2018).

The samples used in this manuscript are sourced from MS lavas (SAS13, SAS14, SAS15) (Harijoko, Milla, et al. 2020) which are Holocene in age, around 4000 to 9000 years BP (Agung Harijoko et al. 2021). The Loyang samples (L1A, L1B, L3, L4, L5, L7, L8, L10, L11) are believed to correspond roughly in age to Slamet's recent Holocene volcanism, being as they are underlain by MS units (Harijoko, Gunawan, et al. 2018). Though Loyang itself has not been

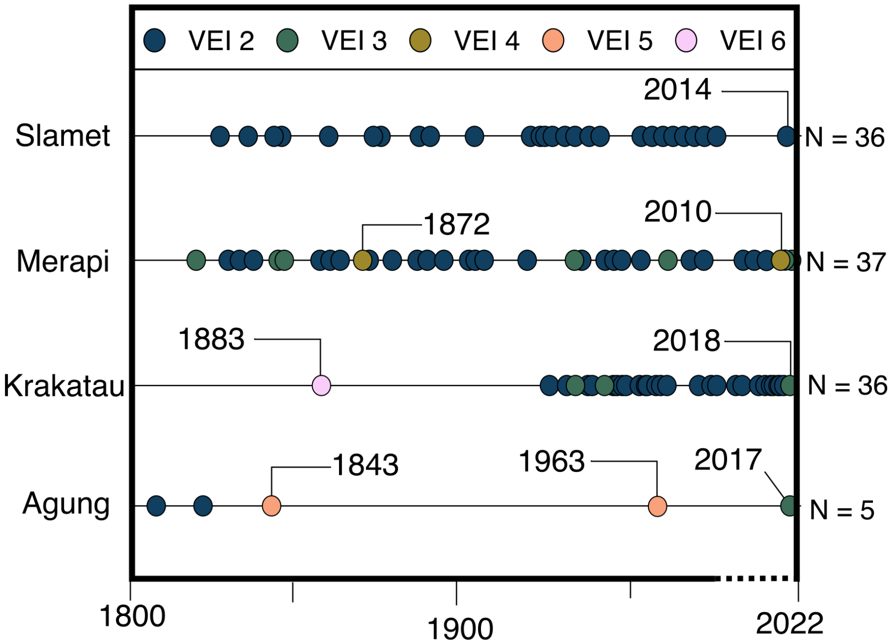

Figure 2: Eruptive history of Slamet and major regional volcanoes Krakatau, Merapi, and Agung, from (Venzke 2013). Slamet has frequent eruptions of (VEI <2) unlike most of its neighbors which have experienced occasional VEI >3 eruptions. Slamet is the only volcano of these four to have significant flank monogenetic volcanism. X-axis is dotted in the bottom right to indicate a time break between the 1950 and 2022 tick, which is longer than the earlier scale of 50 years

age-dated, Gunung Dipajaya (another scoria cone in Slamet's MVF) had one of its scoria bombs K/Ar age-dated to approximately 42 Ky ± 20 Ky (Igan S Sutawidjaja and Sukhyar 2009). The authors of this study argue that based on the remarkably similar depositional and morphometric features of all of Slamet's scoria cones, that a scoria bomb from G. Dipajaya's age date should be taken as representative of all scoria cones ages, including Loyang (Igan S Sutawidjaja and Sukhyar 2009). If this is the case, these Loyang samples have preceded the Slamet samples by several tens of thousands of years. Furthermore, this temporal gap between Loyang and Slamet is smaller than those examined in similar monogenetic-polygenetic edifices like Hauhungatahi and Ruapehu (Cameron et al. 2010), giving us an opportunity to explore monogenetic-polygenetic connections in a more temporally synchronous system.

3 Sample description and analytical methods

Samples were obtained during a 2017 field campaign led by researchers at Universitas Gadjah Mada (Yogyakarta, Indonesia) - see previously published work for more details on this Slamet-Loyang field work (Harijoko, Gunawan, et al. 2018; Harijoko, Noor, et al. 2018; Harijoko, Milla, et al. 2020; Agung Harijoko et al. 2021). Three scoria bombs were obtained from MS - these samples were from loose, unconsolidated and unconstrained modern eruptive products with minimal erosion. Loyang samples have a tight stratigraphic control (Harijoko, Gunawan, et al. 2018), having been obtained from one of two stratigraphic successions on the N and S faces of the scoria cone (see Figure S1). The Loyang material covered a wide range of size and structural cohesiveness, from lapilli and bombs to scoria pellets and unconsolidated ashfalls. In total, 11 samples were obtained from Loyang. Four thin sections were prepared from Slamet's vesicular bomb material to study petrographic relationships. All samples from both Slamet and Loyang were then jaw crushed and sieved into four size fractions (<250, 250–1000, 1–2,000, and >2,000 μm). Portions of the 250–1000 μm size fraction were randomly subdivided, with one fraction used for powdering, and another subset for grain and glass fragment picking. Of those fractions used for grain picking, one portion contained plagioclase, pyroxene, and olivine phenocrysts picked for mineralogical characterization, while another was picked for melt inclusion-bearing olivines and clinopyroxenes. Grain mounts were separately prepared for: (1) each sample in the case of the poly-mineralic picking portions or (2) olivine and pyroxene-hosted melt inclusions. Subsets of melt inclusions were analysed by Raman spectroscopy, Secondary Ion Mass Spectrometry (SIMS), and wavelength-dispersive and electron-dispersive spectroscopy (WDS & EDS) using Cambridge's electron microprobe (EPMA), while those in grain mounts were only analyzed using WDS and EDS.

3.1 Whole Rock Chemistry

Fractions from each sample were powdered by agate ball mill, and then underwent X-Ray Fluorescence analysis at the University of Leicester. These samples were analysed on the Department of Geology's PANalytical Axios Advanced XRF spectrometer. Major elements from each sample were measured from fused glass beads prepared from ignited powders. The sample to flux ratio of these beads was 1:5, 80% Li metaborate: 20% Li tetraborate flux; results were quoted as component oxide weight percent, and re-calculated to include LOI. Trace elements were analysed on 32mm diameter pressed powder briquettes prepared from ca. 7.5g fine ground powder mixed with ca. 20-25 drops 7% PVA solution and pressed at 10 tons per square inch. Loss-on-emission (LOE) sample weights for ash samples were corrected for using calculated and measured Rh Ka Compton peak intensity.

3.2 Melt Inclusion Preparation

Melt inclusion preparation in this study followed the methods of prior studies in our research group (Wieser et al. 2021) as well as best practices in the field (Rose-Koga et al. 2021). Olivine and pyroxene-hosted melt inclusions were imaged using optical microscopy during the picking process. Individual crystals were prepared for analysis by mounting them on glass slides using CrystalBond. They were then hand-polished using 250—7000 grit papers (progressively decreasing degree of coarseness) until each melt inclusion was within 10 μm of the surface. Unbreached melt inclusions were then analyzed using Raman spectroscopy at the University of Cambridge (see section below for analytical details). After Raman analysis, each olivine was re-polished to expose the melt inclusion at its maximum diameter. Olivines were carefully extracted from crystal bond using acetone, and remounted for SIMS analysis (see section below for analytical details) at the Edinburgh Ion Microprobe Facility (EIMF; University of Edinburgh). Prior to SIMS analysis, melt inclusion mounts were bulk-polished using Cambridge's Saphir polishing rigs at 9, 6, 3, 1, and 1/4 μm polishing grades in increasing order of fineness using diamond suspension pastes. After fine polishing, these mounts were gold-coated. Finally, after SIMS analysis, the mounts were re-polished using the Saphir rigs to remove the gold coat, and carbon-coated for EPMA analysis and back-scatter electron (BSE) imaging; see EPMA section for analytical details. A total of 33 melt inclusions from both Slamet (n=7) and Loyang (n=24) were analysed. Generally, Slamet phenocrysts had poorly preserved melt inclusions.

3.3 Analytical Procedures

3.3.1 Raman Analyses of Melt Inclusion Vapor Bubbles

Raman spectroscopy was used to assess whether the vapour bubbles present in these melt inclusions contained significant quantities of CO_2. These vapour bubbles have been shown to be effective reservoirs of CO_2, holding as much as 50% of a melt inclusion's CO_2 (Wieser et al. 2021; Lamadrid et al. 2017; Rasmussen et al. 2020). Studies using Raman spectroscopy integrated with traditional volatile techniques like Fourier-transform infrared spectroscopy (FTIR) and/or SIMS, have shown that pressures estimated from melt inclusion CO_2 content may be severely underestimated if vapour bubble CO_2 is not considered (Lamadrid et al. 2017; Wieser et al. 2021; Rose-Koga et al. 2021). Our Raman methodology followed previously reported method development at Cambridge (Wieser et al. 2021). The goal of Raman analyses was to estimate CO_2 concentrations in melt inclusion-hosted vapour bubbles. After vapor bubbles were identified visually, crystals were hand-polished to around 5000 grit individually to within 10 μm of the crystals surface to avoid exposing the vapor bubble.

These vapour bubbles were measured using a confocal LabRAM 300 (Horiba Jobin Yvon) Raman spectrometer in the Department of Earth Sciences at the University of Cambridge. After subtracting the background signals, the position of Fermi diad peaks (whose separation correspond to the density of CO_2 inside the vapor bubble) were measured using a polynomial peak fitting script written for MATLAB (Lamadrid et al. 2017; Fermi 1931; Wieser et al. 2021). Peak correction and calibration was performed using a series of standards including synthetic fluid-inclusions (Wieser et al. 2021) entrapped in quartz and high-CO_2 vapour bubbles in MIs from Kilauea (Wieser et al. 2021). Following analysis of Raman spectra, CO_2 density was estimated using a calibrated densimeter calibrated specifically for this Raman spectrometer (Wieser et al. 2021). Briefly, the calibration procedure will be outlined here. The fermi diad separation (Δ) was related to known standards of varying CO_2 density (ρ_{CO_2}). The densimeter line was calculated by applying a linear regression with 95% confidence intervals to the calibration data set (Wieser et al. 2021):

$$\rho_{\mathrm{CO_2}}\left(\mathrm{g/cm^3}\right) = 0.3217 \pm 0.026\Delta\left(\mathrm{cm^{-1}}\right) - 32.995 \pm 2.7 \tag{1}$$

The resulting densities were then converted to measurable CO_2 concentrations (ppm). This requires knowledge of both the vapor bubble and its parental melt inclusion's volume, which were approximated optically:

$$[\mathrm{CO_2}]^{VB} = 10^6 \times \frac{\rho_{\mathrm{CO_2}} V_{VB}}{\rho_{\mathrm{Melt}}\, V_{\mathrm{Melt}}} \tag{2}$$

Where V_{VB} and V_{melt} correspond to the volume of the vapor bubble and melt inclusion in cm^3, respectively (Wieser et al. 2021). This step contributed most to the uncertainty on the amount of CO_2: we assume that measured elliptical axes of our melt inclusion correspond to to a roughly spherical volume. While this step makes large assumptions, only two of our Slamet or Loyang melt inclusions had any measurable CO_2 in the vapor bubble, so this volume uncertainty does not affect the majority of our reported CO_2 concentrations. The resulting vapor bubble CO_2 is added to our melt inclusion CO_2, determined by SIMS (see next section).

3.3.2 Scanning Electron Microscopy (SEM)

Prior to SIMS analysis, the uncoated melt inclusion-bearing grain mounts were analyzed for back-scatter electron (BSE) images on the FEI Quanta 650FEG scanning electron microscope (SEM) at the University of Cambridge in low vacuum mode. After SIMS analysis, carbon-coated melt inclusions, grain mounts, and thin sections were imaged in high vacuum mode under the following conditions: 10 kV, aperture size 4. Thin sections were carbon-coated and analyzed using QEMSCAN under high vacuum conditions at 20 kV and aperture size 4. The proportions of major mineral phases composing these thin sections were determined by coloring major phases for a primary cation e.g., coloring plagioclase for Ca. These "greyscale" values were then segmented using the software ImageJ to determine the relative proportion of each phase.

3.3.3 Secondary Ion Mass Spectrometry (SIMS)

Following Raman analysis and the creation of epoxy grain mounts, the concentrations of H_2O and CO_2 in melt inclusions were obtained using the Cameca IMS-7f GEO at the Edinburgh Ion Microprobe Facility (EIMF; University of Edinburgh). Due to COVID-19 related access restrictions, all analyses were performed by Dr. Cees-Jan de Hoog. SIMS analysis was performed prior to EPMA to maximize the signal and to avoid contamination of measured carbon concentrations by a carbon coat (Wieser et al. 2021). Epoxy grain mounts were subjected to a beam of primary $^{16}O^-$ ions with the following beam conditions: 5 nA, 18 kV spot size of 10 μm. Standards analyzed included M5, M40, M36, M10, 519-4-1, and N72, which were analyzed before, during, and after SIMS runs. See Supporting Information for more SIMS calibration and run information.

3.3.4 Electron Microprobe EPMA

EPMA was conducted using a Cameca SX100 EPMA in the Department of Earth Sciences, University of Cambridge. Two analytical procedures were followed - one for whole crystals, and one for melt inclusions. See Supplementary Materials for full details. For olivine crystals (i.e. those without melt inclusions), analyses were taken using a 15keV and 40nA focused (1 μm) beam. Glass analyses (both MIs and groundmass glass) were run on 15 keV and 10nA defocused (10 μm) beam.Count times and calibration materials are shown in

Supplementary Materials (Tables S2-5). San Carlos olivines, as well as known standard grains of augite, plagioclase, and basaltic glass (VG92) were used as secondary standard compositions, and were run at the beginning and end of each analytical run. For individual crystals, analyses included core, rim, and profile measurements. For melt-inclusion bearing crystals, melt inclusions were analyzed using the glass-settings file conditions found in Table S2. Melt inclusions were analyzed individually and where possible multiple times to obtain better statistics. A subset of melt inclusion-free olivines were analyzed for high resolution Ni data, using a higher LIF crystal count time for Ni (100s) as opposed to the normal procedure (40s).

4 Modeling Methodologies

The methods used to model processes like post-entrapment crystallization, fractional crystallization (combination of rhyolite-MELTS (G. A. Gualda et al. 2012) and mass-balance modeling), melt inclusion saturation pressures (Iacovino, Matthews, et al. 2021), and hierarchical cluster analysis (Boschetty et al. 2022) are discussed in detail in the Supplement.

5 Results

5.1 Whole Rock Compositions

Chemical compositions of sample powders can be found in Table 1, and reported in Figures S2 and 3. Analytical totals for samples were all above 99%, and below 100.30 %; LOI was similarly low, with only one sample (L7) above or below 2%. All samples are basaltic to basaltic andesitic (Bas et al. 1986) following Total-Alkali Silica diagrams, with whole rock MgO $>$ 4 wt.%, consistent with earlier analyses on similar sample sets (Harijoko, Noor, et al. 2018; Harijoko, Milla, et al. 2020). With such low LOI, it is unlikely any trace element enrichment is due to alteration or weathering, consistent with the fresh appearance of most samples.

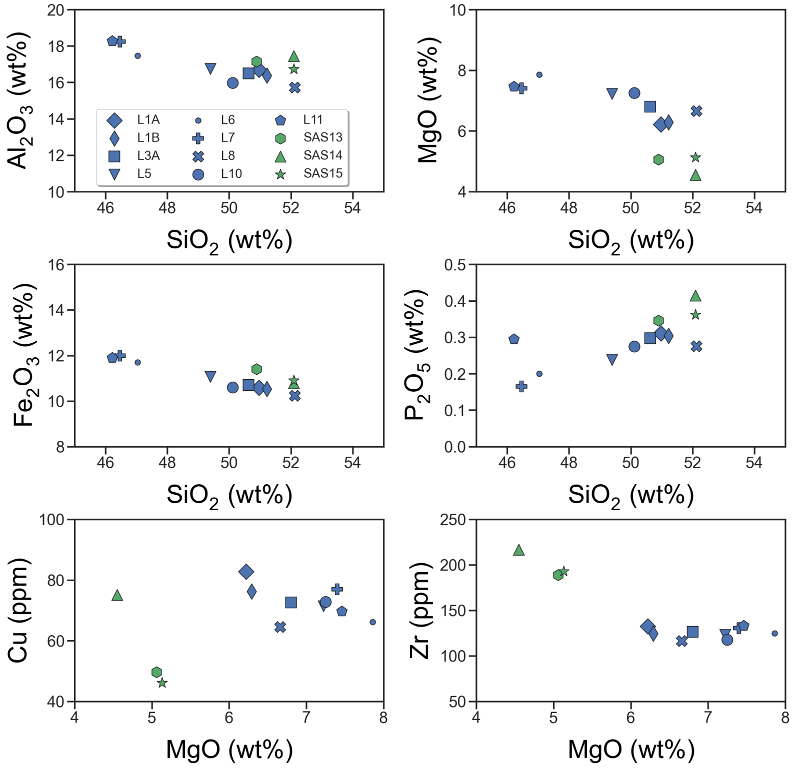

Figure 3: Whole rock chemistry of major elements (a-c) and trace elements (d-f) in Loyang and Slamet samples.

Table 1: Whole rock geochemical data for both Slamet and Loyang.

Fe_2O_3 has been converted to FeO in following analyses

	Loyang									Slamet		
	L1A	**L1B**	**L3A**	**L5**	**L6**	**L7**	**L8**	**L10**	**L11**	**SAS13**	**SAS14**	**SAS15**
SiO_2	51.0	51.2	50.6	49.4	47.0	46.5	52.1	50.1	46.2	50.9	52.1	52.1
TiO_2	1.35	1.34	1.34	1.36	1.41	1.48	1.27	1.31	1.48	1.57	1.47	1.44
Al_2O_3	16.7	16.4	16.5	16.8	17.5	18.2	15.7	16.0	18.3	17.2	17.5	16.7
Fe_2O_3*	10.6	10.5	10.7	11.1	11.7	12.0	10.2	10.6	11.9	11.4	10.8	10.9
MnO	0.17	0.17	0.17	0.17	0.18	0.19	0.16	0.17	0.16	0.18	0.18	0.18
MgO	6.22	6.29	6.80	7.22	7.86	7.40	6.66	7.25	7.46	5.06	4.55	5.13
CaO	9.46	9.56	9.93	9.89	9.98	9.61	9.52	10.13	9.88	8.76	8.71	8.59
Na_2O	2.90	2.84	2.77	2.38	2.20	2.05	2.65	2.63	2.27	3.38	3.58	3.26
K_2O	1.21	1.17	1.12	0.80	0.40	0.30	1.06	1.02	0.46	1.15	1.37	1.26
P_2O_5	0.311	0.304	0.297	0.238	nd	0.165	0.276	0.275	0.295	0.346	0.415	0.362
SO_3	0.002	nd	nd	0.030	nd	nd	nd	nd	nd	nd	nd	nd
LOI	0.13	0.08	nd	0.85	1.32	2.31	0.02	0.20	1.64	0.22	nd	nd

	L1A	**L1B**	**L3A**	**L5**	**L6**	**L7**	**L8**	**L10**	**L11**	**SAS13**	**SAS14**	**SAS15**
Total	100.02	99.88	100.15	100.15	99.76	100.21	99.69	99.68	100.04	100.11	100.38	99.90
As	nd	1.0	1.5	nd	nd	nd	nd	1.0	nd	1.5	2.6	1.6
Ba	209	201	198	203	207	288	190	188	191	200	242	226
Ce	40.6	39.9	37.4	36.7	38.9	39.4	34.6	33.7	42.5	37.5	50.9	44.7
Co	39.0	37.8	38.3	41.1	45.6	44.9	39.2	40.3	43.5	37.0	32.5	36.4
Cr	93.8	103	120	133	138	149	114	151	133	28.2	21.5	32.0
Cs	nd	nd	2.5	3.5	3.9	nd	nd	3.2	nd	3.0	nd	2.1
Cu	82.8	76.2	72.6	71.4	66.2	76.9	64.6	72.8	69.7	49.7	75.1	46.1
Ga	18.5	18.5	19.1	19.0	19.6	21.4	17.1	18.0	19.6	21.0	20.5	19.1
La	16.2	16.1	18.8	17.3	17.5	17.3	17.1	15.0	18.6	17.6	21.2	21.4
Mo	2.2	1.9	2.6	2.0	1.7	1.6	2.3	2.1	1.8	2.6	3.1	2.5
Nb	10.9	10.0	10.2	10.1	10.0	10.3	9.5	9.7	10.6	14.5	15.9	14.5
Nd	21.8	21.0	20.3	22.2	21.1	21.9	20.3	17.6	21.5	20.5	26.2	22.3
Ni	37.8	34.3	41.9	50.5	58.0	52.7	46.2	51.8	49.2	8.5	7.5	14.9
Pb	6.2	6.8	8.2	6.4	7.1	5.1	5.3	6.4	5.4	8.1	9.9	6.9
Rb	30.0	29.2	28.5	23.6	10.3	8.0	26.3	25.7	9.3	29.2	35.8	33.7

	L1A	**L1B**	**L3A**	**L5**	**L6**	**L7**	**L8**	**L10**	**L11**	**SAS13**	**SAS14**	**SAS15**
Sb	nd	nd	nd	nd	nd	nd	nd	nd	nd	nd	nd	nd
Sc	35.2	34.9	37.2	35.6	40.5	40.2	33.4	40.2	39.7	32.0	27.3	27.7
Se	nd	nd	nd	nd	nd	nd	nd	nd	nd	nd	nd	nd
Sn	1.3	nd	nd	nd	nd	nd	nd	nd	nd	nd	1.3	3.2
Sr	352	333	354	359	367	374	344	349	345	293	321	315
Th	4.7	4.4	4.4	4.3	4.6	4.5	3.6	3.7	4.1	5.1	5.9	5.3
U	0.8	1.0	1.1	0.8	1.0	0.6	nd	nd	nd	1.1	1.8	1.2
V	285	283	284	252	263	244	278	287	287	252	226	251
W	nd	nd	nd	nd	nd	nd	nd	nd	nd	nd	2.7	nd
Y	27.9	26.6	27.6	27.9	29.0	28.6	26.8	27.3	30.0	34.5	38.3	34.5
Zn	82.1	72.0	75.8	77.5	80.5	83.8	71.2	74.6	77.3	90.5	86.3	83.2
Zr	132	125	126	123	125	131	116	118	133	189	217	193
Ba/Nb	19.1	20.1	19.3	20.2	20.6	27.8	20.0	19.4	18.0	13.8	15.2	15.6
Pb/Nd	0.28	0.33	0.40	0.29	0.33	0.23	0.26	0.37	0.25	0.39	0.38	0.31
Zr/Nb	12.2	12.4	12.4	12.3	12.4	12.7	12.2	12.2	12.6	13.1	13.7	13.3
Sr/Y	12.6	12.5	12.8	12.9	12.6	13.1	12.8	12.8	11.5	8.5	8.4	9.1

5.2 Sample Petrography

Four thin sections were prepared from three separate volcanic bombs at Slamet. The Slamet thin sections contain phenocrysts of plagioclase (plag), augite (cpx), olivine (ol) and ti-magnetite (mag). Plagioclase crystals range in size from microlites up to 1 cm; cpx and ol both tend to be smaller, subequant to anhedral, generally less than 0.5 cm. Glomerocrysts (composed primarily of pyroxenes + olivine ± ti-magnetite) of up to 1 cm in size are relatively common (see Figure 4a). Rounded and heavily resorbed olivines host cpx inter-growths in some cases (Figure 4b). Melt inclusions are also common in many olivines (Figure 4c). Clinopyroxene often contains inclusions of other minerals, such as opaque oxides, plagioclase, and other minor phases; in some cases, equant clinopyroxenes show evidence of overgrowing earlier-formed plagioclases (Figure 4d). Many crystals, especially plagioclase and olivine, show complex zoning patterns; see Figure 4e and the thin section QEMSCAN Figure S3 for representative plagioclase zoning and sieve textures, and Figure 6c-e for olivine zoning. The groundmass in Slamet thin sections is dominated by plagioclase and minor amounts of clinopyroxene ± olivine; in some cases, plagioclase microlites show weak alignment (Figure 4e-f). QEMSCAN maps of the thin sections like SAS14a provide quantitative estimates of abundance of major phenocryst phases - these are reported in Table 2, and is shown in 15 μm resolution QEMSCAN maps in Figure S3. Across the four Slamet sections analyzed, there are no major differences in the modal abundance of major phases, with the exception of Ti-magnetite in SAS15, whose abundance is 50% lower than comparable magnetite populations SAS14 or SAS13. Loyang samples, made of lapilli and scoria, were not assessed to the same level of petrographic detail as Slamet samples. However, published work on Gunung Loyang (Harijoko, Gunawan, et al. 2018; Harijoko, Milla, et al. 2020) has found that dominant phenocryst phase is plagioclase (Harijoko, Milla, et al.

2020), followed by minor amounts of olivine, clinopyroxene, orthopyroxene, and opaque minerals (Harijoko, Gunawan, et al. 2018). Such mineral abundances are similar to those observed in Slamet. However, phenocrysts constitute a small relative percentage (5%) of Loyang scoria, where nearly 45-50% of each sample is composed of groundmass glass, and another 45-50% is composed of vesicles (Harijoko, Gunawan, et al. 2018). The vesicularity of Loyang material peaks in the middle stages of its eruptive sequence (L3-L8), which has been interpreted to represent a higher degree of explosive, Strombolian style eruptions at this time (Harijoko, Gunawan, et al. 2018). Some Loyang samples exhibit a trachytic texture dominated by microlite plagioclase (Harijoko, Milla, et al. 2020).

Table 2: Proportions of major phases in terms of their modal mineralogy. Obtained from QEMSCAN data.

	SAS13	SAS14A	SAS14B	SAS15
Plagioclase(%)	35.7	38.7	36.9	34.4
Clinopyroxene (%)	4.8	4.3	3.6	4.0
Olivine (%)	4.4	3.3	3.8	5.6
Ti-Magnetite (%)	2.6	2.4	2.4	1.3
Total phenocryst (%)	**50.2**	**53.9**	**51.7**	**48.7**

5.3 Mineral Chemistry

5.3.1 Olivines

We conducted over 1100 EPMA measurements on >200 olivines from both Slamet and Loyang (see Figure 5, 7, and 8a-d for olivine core chemistry), including over 600 EPMA profile points of 20+ olivines providing high-resolution

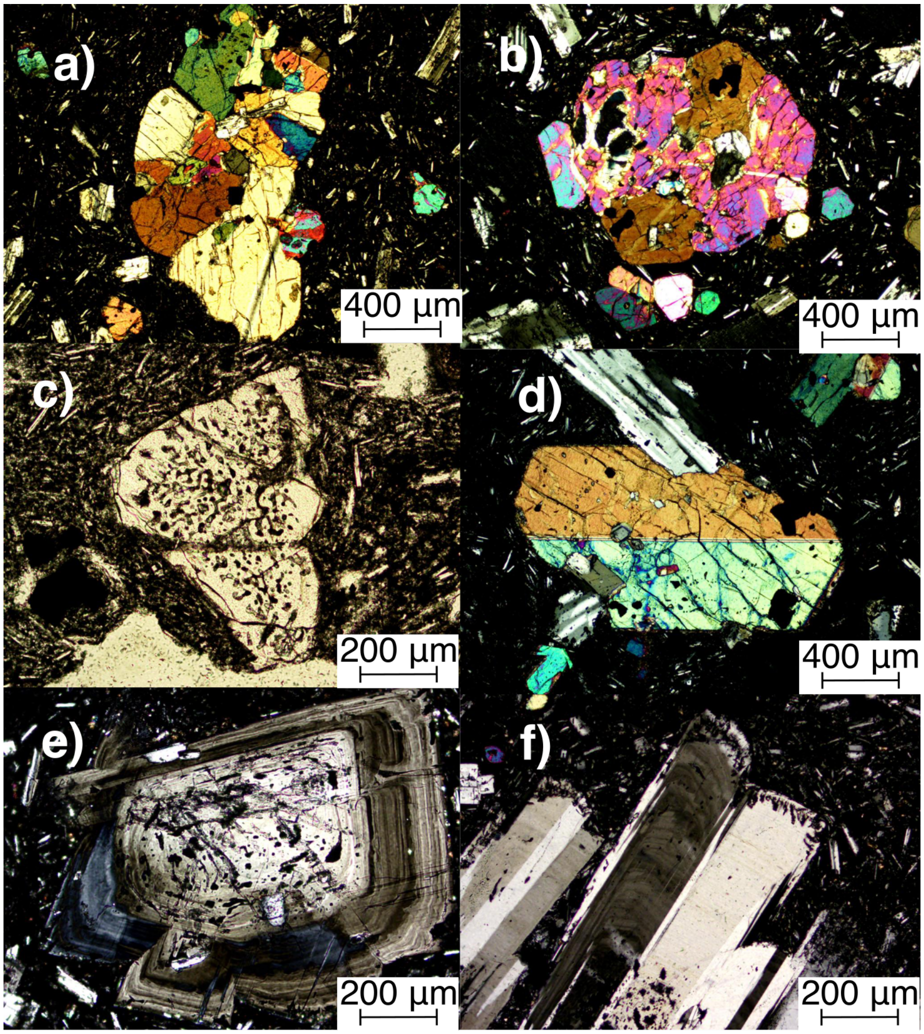

Figure 4: a) Glomerocryst of olivine, pyroxene, and plagioclase, from SAS13. b) Clinopyroxene (cpx) inter-growth with resorbed olivine. from SAS15. c) Melt and fluid inclusion trails in olivine clot, which also shows evidence of olivine resorption (Type 2), from SAS14a. d) Twinned, well-formed cpx growing with elongate plagioclases, from SAS 14a. e) Equant, oscillatory zoned plagioclase with a sieved core, from SAS15. f) Close up view of tabular, zoned, and twinned plagioclase crystals. The large crystals are surrounded by glass and microlites of plagioclase showing weak alignment.

spatial and chemical zoning data (see Figure 8e-j for representative summaries). All of these data are reported in the Supplementary Material as a CSV file. This large database of olivine compositions, along with representative BSE images of olivines from both Slamet and Loyang (see Figure 6 for summary) allows detailed comparisons to be made between the crystal cargoes erupting from each volcanic centre. We focus on olivine phenocrysts as the primary mineral phase of interest in these systems, as the complexities of melt-olivine interactions are much better experimentally-constrained than other phases (Roeder and Emslie 1970; Beattie, Ford, and Russell 1991; Li and Ripley 2010; Rose-Koga et al. 2021). Olivine phenocrysts are a minor but important phase throughout the Slamet samples (see Figures 4a-c and S3).

Large olivine phenocrysts are generally more euhedral than smaller crystals. There are also abundant olivine microcrysts in the groundmass; these are equally abundant across the thin sections. QEMSCAN phase maps (Figure 5) and EPMA analyses of Loyang and Slamet olivines (Figure 8e-j) show that zonation is relatively common for olivines in both systems. This zonation is both normal (forsterite content (Fo), the relative proportion of Mg vs. Fe in olivine), decreases with distance from crystal core) and reverse (Fo increases with distance from crystal core) in different populations of olivines. Furthermore, BSE images of olivines from Loyang and Slamet showcase this zonation and different degrees of resorption well. Interconnected networks of inclusions are common in zoned olivine phenocrysts (Figure 4c), evident in optical microscopy and BSE images. The latter technique was also used with Loyang olivines, where those crystals which exhibit zonation also commonly bear fluid inclusions and demonstrate edge resorption. These textures are very rare in the homogeneous olivines both from Slamet and Loyang. High resolution EPMA profiles of select olivine phenocrysts shown in Figure 8e-j also reveal consistent zoning in nickel (Ni),

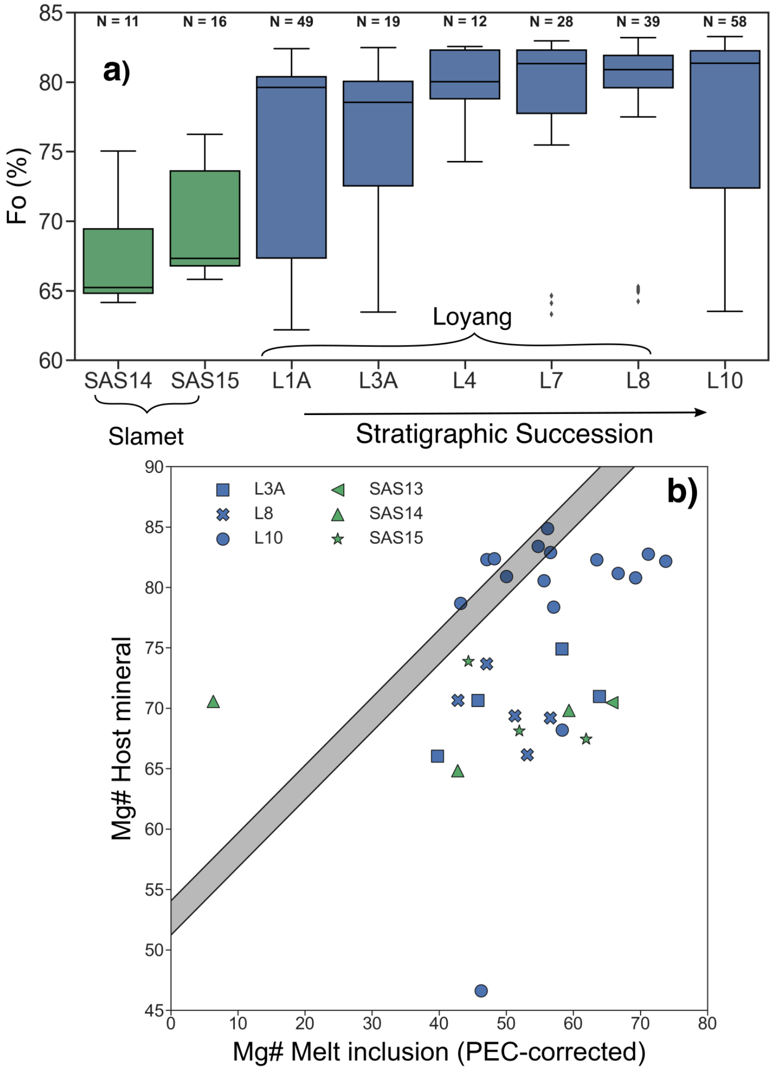

Figure 5: a) Box plot showing olivine core Fo. content for Slamet (SAS) and Loyang (L) olivines. Loyang olivines are stratigraphically ordered from oldest (L1) to youngest (L10); b) Roeder (Roeder and Emslie 1970) plot showing olivine Mg# compared to melt inclusion Mg# in same olivines. Equilibrium olivine composition (grey bars) estimated by Fe-Mg exchange coefficient 0.30 +/- 0.03 (Roeder and Emslie 1970)
.

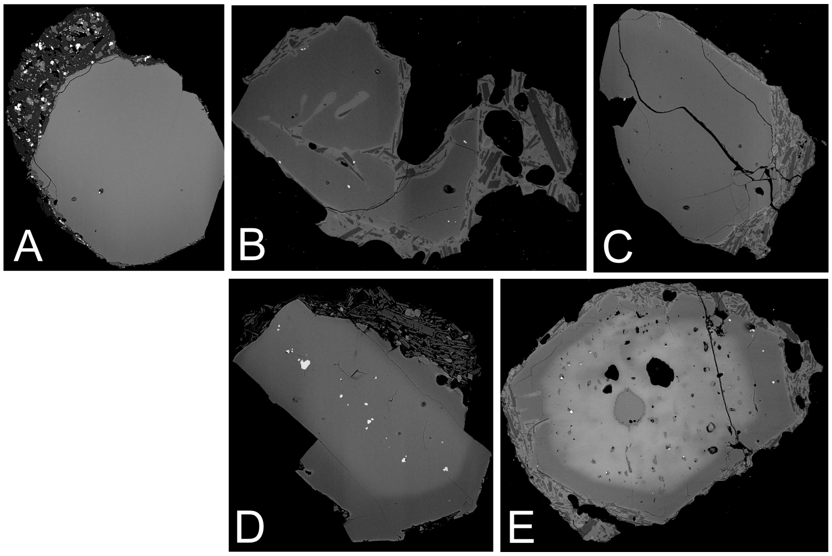

Figure 6: Classification scheme for olivines analyzed in this study. See text for more details. Each panel shows a representative example of each olivine sub-population: a) Type 1 olivines, which are homogeneous and unresorbed; b) Type 2 olivines are homogeneous and show mild resorption with no zoning; c) Type 3 olivines show normal zoning (mafic core, evolved rim); d) Type 4 olivines show minor reverse zoning (evolved core, mafic rim); e) Type 5 olivines show extreme reverse zoning

which is a useful element for understanding the timescale and thermal conditions affecting an olivine during and after growth (Li and Ripley 2010; Gordeychik, Churikova, Shea, et al. 2020; Straub et al. 2008; Gordeychik, Churikova, Kronz, et al. 2018). These olivine textural and chemical systematics have allowed us to develop an olivine classification scheme shown in Figure 6, which will be discussed in the Discussion section in greater detail.

5.3.2 Pyroxene

A summary of Slamet and Loyang's pyroxene chemistry can be found in Figure S4a. All but one Slamet pyroxene plots in the augite field, with one Slamet pyroxene standing out as an orthopyroxene (Figure S4a). Loyang has all but two pyroxenes plotting in the clinopyroxene field; of these, about half plot in the diopside field, while the other half in the augite field (Figure S4a). In Figure S4b, we can see that Loyang pyroxene cores show a decreasing molar Mg#, where Mg# is defined as:

$$Mg\# = \frac{Mg}{Mg + Fe_t} \tag{3}$$

trend with stratigraphic height, where L10 preserves the most Fe-rich pyroxenes. Few of the pyroxene cores measured are in equilibrium with their host melt, as evidenced by the offset in core/rim Mg# (Figure S4c). In several cases, pyroxene crystals intergrow with and resorb olivine phenocrysts (Figure S3b), and they are often found in glomerocrysts (Figure S3a). Microphenocrysts of pyroxene can be observed in Slamet's glasses. Many pyroxenes contain inclusions, both of opaque oxides and melt inclusions. Among those pyroxenes hosting melt inclusions, there are abundant inclusions of opaque oxides, spinels, and sulfides.

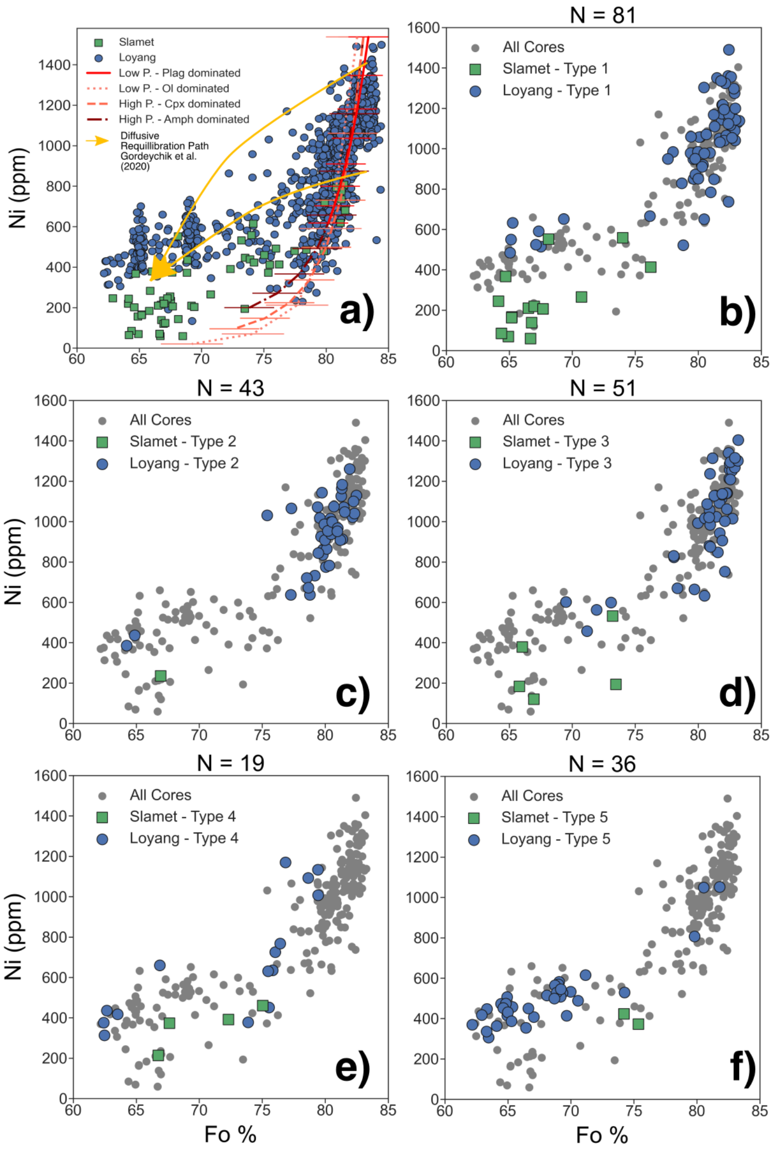

Figure 7: a) Ni vs. Fo trends in olivine cores (a) from Slamet (green) and Loyang (blue) alongside mass balance curves. a) Also includes schematic representation of diffusive requilibration's effect on Ni and Fo, from (Gordeychik, Churikova, Shea, et al. 2020; Gordeychik, Churikova, Kronz, et al. 2018). See text for more details on mass balance model. Ni partitioning model in olivine from (Li and Ripley 2010); b) throguh f): Forsterite content (Mg/Mg + Fe) of olivine cores vs. Ni content of olivine cores in Slamet and Loyang. Different panels correspond to a) the whole core dataset and b-f) the different "types" of olivines identified in Figure 6 and discussed in the text.

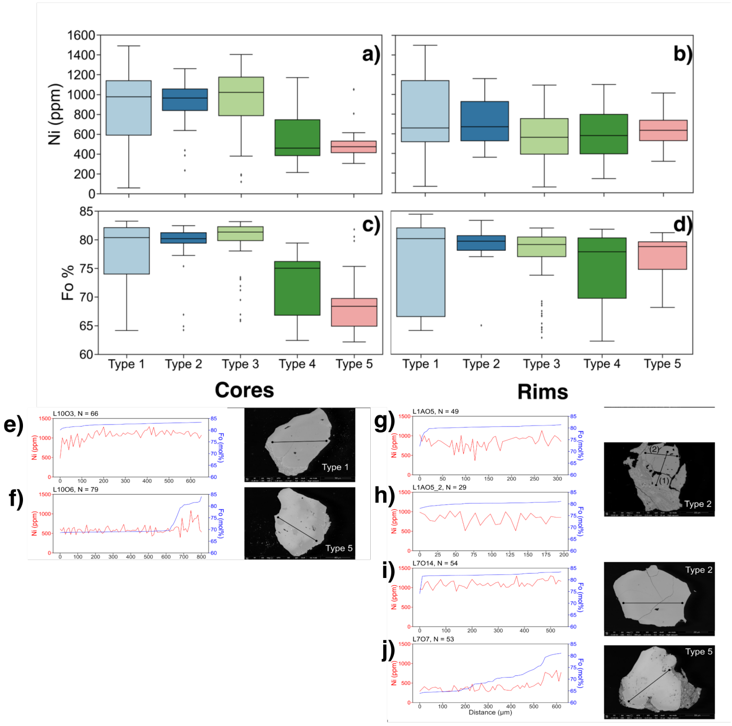

Figure 8: a) through d): Box and whisker plots showing distribution of Fo and Ni across different olivines. Comparison of Fo content (%) and Ni (ppm) in olivines cores vs. rims. Each box corresponds to one of the five olivine groups defined in Figure 5; e) through j): Ni and Fo profiles of select Loyang olivines. Profiles were taken from those olivines which typified homogeneous (Type 1 and 2) and reverse zoned (Type 5) groups. See text for discussion of olivine classification scheme.

5.3.3 Plagioclase

Plagioclase is the dominant phenocryst phase in the Slamet sections (Table 2), as shown in the representative QEMSCAN image of thin section SAS14A from Slamet (Figure S3). Plagioclase microlites (generally andesine in composition) are abundant in the groundmass (Figure 4e, f and FIgure 5). The microlites demonstrate a greater extent of grain alignment than the larger phenocrysts (Figure 4), which may indicate a preferential orientation of stress. However, such alignments are not reflected in vesicle textures (Figure 4). Almost ubiquitously, the plagioclase phenocrysts are sieve-textured and demonstrate clear growth zones, evident under both optical microscopy (Figure 4) and by QEMSCAN (blue coloration in Figure S3 reflects degree of anorthite content or molar An%, which is defined as:

$$An\% = \frac{Ca}{(Ca + Na + K)} \tag{4}$$

Plagioclase from Loyang samples shares similar textural features to Slamet, but in our sample set Loyang feldspars are less common than has been reported in the literature (Harijoko, Noor, et al. 2018). As such, we only report core and rim compositions of plagioclases from Slamet in Figure S5, and argue that these compositions are representative of Loyang as well, given the textural similarity between the two centres observed in previous studies (Harijoko, Noor, et al. 2018). All of Slamet's feldspars plot in the bytwonite-labradorite ($An_{80} to An_{58}$), and feldspar cores show weak disequilibrium with their rims (Figure S5).

5.4 Cluster Analysis

The results of our hierarchical clustering models are shown in Figure S6, based on olivine core compositions from both Slamet and Loyang. Figure S6 shows the structure of our clustering analyses after log-ratio transformations (see Methods for details) represented a a dendrogram. This plot indicates that at higher levels, four clusters are detectable among our olivine core compositions. Running the hierarchical clustering algorithm (following (Boschetty et al. 2022)) results in four statistically distinct clusters (Figure S7). These clusters vary from mafic (Ol1) to evolved (Ol4) across all six elements (Si, Mg, Fe, Ca, Mn, Ni) included in our database (see Table 3, Figure 9). Cluster Ol1 is dominant in all Loyang samples with the exception of L3 (see Figure 10b), while Cluster Ol4 is dominant in all Slamet olivines. L3 has the largest proportion of Ol2 and Ol4 clustered olivines among the Loyang samples. Generally, the number of Ol1 vs. Ol4 clusters does not vary systematically from oldest (L1) to youngest (L10) Loyang samples. Among the texturally-identified olivine types in our dataset, there is a strong overlap between both textural and clustering schemes e.g., Ol3 and Ol4 predominate in both Type 4 and Type reverse-zoned olivines (Figure 10a). The implications of these results will be discussed more in the next section. Following a bootstrapping method (described in the original manuscript), we found that for our olivine core dataset, the "robustness" of our clustering scheme was 87% +/− 0.2 SD (see Methods section for details).

Table 3: Representative compositions of the four olivine clusters identified using the Boschetty machine-learning cluster algoirthm (Boschetty et al. 2022)."Representative" compositions were selected to most closely match the average cluster composition. All oxides are reported in wt.%

Cluster	Sample	SiO_2	TiO_2	Al_2O_3	Cr_2O_3	FeO	CaO	MgO	MnO	NiO
Ol1	L10 O3	39.46	0.008	0.019	0.003	17.48	0.16	43.12	0.22	0.1338
Ol2	L3 O14	38.99	0.020	0.017	0.022	19.48	0.22	40.99	0.31	0.0931
Ol3	L1A O3	38.23	0.044	0.035	0.018	24.79	0.17	37.23	0.39	0.0762
Ol4	L1A O29	36.94	0.052	0.030		30.11	0.22	32.45	0.48	0.052

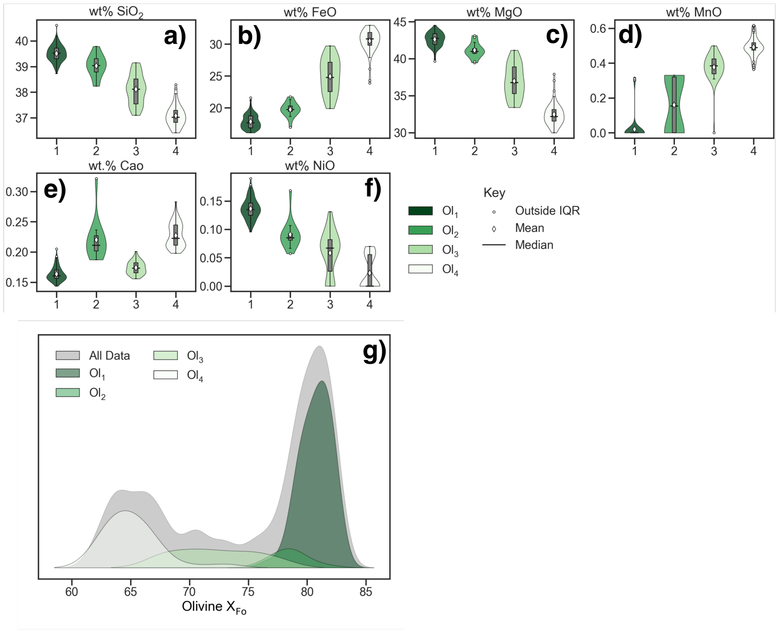

Figure 9: a) through f): Violin plots showing the composition of each of the four olivine core clusters identified using hierarchical clustering methods (see text for details). Each component used to determine the clusters is shown, with statistical details (median, mean) reported; g) Kernel density estimate (KDE) showing the distribution of Fo content within each olivine cluster. See text for details.

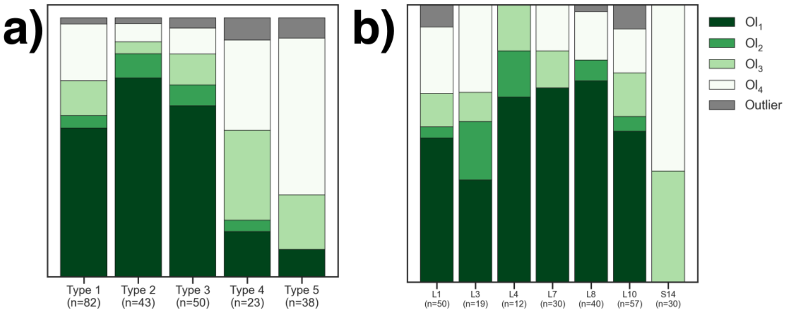

Figure 10: a) Stacked bar charts showing the relative proportion of each olivine's assigned cluster within a texturally defined olivine "Type," as described in the text and in Figure 6; b) Stacked bar charts showing the relative proportion of each olivines assigned cluster within a given sample.

5.5 Melt Inclusions

In all, 33 melt inclusions from Slamet (n=7) and Loyang (n=24) were imaged under optical microscopy, and measured with Raman, SIMS, and Electron Probe. These represent the first melt inclusion analyses reported for this system. The melt inclusion compositions are plotted on a 'total alkalis-silica' diagram (Bas et al. 1986), along with the calibration glasses used in the saturation pressure software VESIcal in Figure S8. The major and trace element chemistry of melt inclusions (corrected for PEC) are reported for both of the volcanoes are shown in Figure S9. After Raman analysis, it was found that only two of the 33 melt inclusion shrinkage bubbles (L104 and S303B) contained CO_2 diads. Unfortunately, L104's melt inclusion CO_2 concentration could not be measured, so we only report the vapor-bubble-corrected CO_2 concentration of S303B (Figure S10-11) The volatile contents measured by SIMS are plotted in Figure 11, colored for both host Mg# and PEC%. Measured CO_2 and H_2O concentrations are less than 2500 ppm and 4 wt.%, respectively. Figure 11a also shows calculated isobars (i.e. entrapment pressures) for the 33 analyzed melt inclusions, using the VESICal package based on the MagmaSat saturation pressure model (Iacovino, Guild, and Till 2020; Ghiorso and G. Gualda 2015). Compilation plots showing the volatile contents plotted against corresponding saturation pressure are provided in Figure S10. Finally, the evolution of entrapment pressures with Loyang stratigraphy is presented in Figure S11, alongside selected images of some of the highest CO_2 concentration melt inclusions.

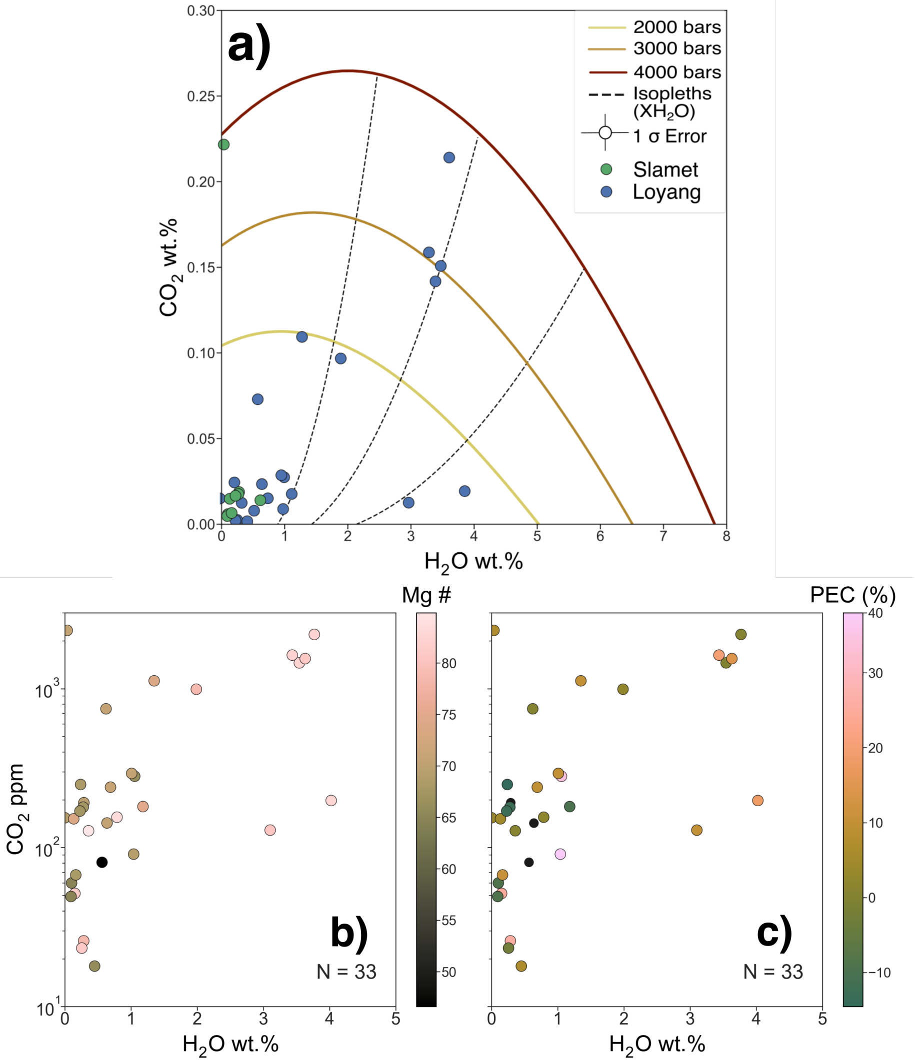

Figure 11: a) CO_2 and H_2O contents of melt inclusions plotted with MagmaSat estimated isobars and isopleths (Ghiorso and G. Gualda 2015; Iacovino, Matthews, et al. 2021). Degassing paths of L109A melt inclusion (highest CO_2 measured) are also shown; b) Melt inclusion volatile contents: CO_2 in ppm. H_2O in wt.% colored for host mineral Mg# (either cpx or olivine); c) Same as (b), colored for PEC. Color bars used are batlow and turku, both from from Scientific Color Maps (Crameri 2019)

6 Discussion

6.1 Bulk rock chemistry controlled by fractional crystallization

Loyang and Slamet's whole rock compositions are basaltic to basaltic-andesite (Figure S2). They are shown to follow a basaltic differentiation trend during fractional crystallization (FC) based on our rhyoliteMELTS (G. A. Gualda et al. 2012; Ghiorso and G. Gualda 2015) differentiation model curves in Figure S2 (see Methods section for model details). The "dry" model was run in the absence of any water, resulting in a liquidus temperature of 1238°C and producing abundant plagioclase and clinopyroxene as main phenocryst phases, as well as minor amounts of orthopyroxene, spinel, and Fe-oxide. The "wet" model, by contrast, has starting H_2O content of 3.0 wt%. This results in a lower liquidus temperature of 1169'°C. Spinel and clinopyroxene form the bulk of the solid assemblage in this model, followed by minor amounts of plagioclase and Fe-oxide. Neither model produced olivine, an important mineral in this system, nor did either curve perfectly reproduce the linear differentiation seen in Figure S2 and Figure 3. However, the relative magnitude of evolution captured in both curves is suggestive of a somewhat hydrated source melt differentiating under mid-crustal (<10 km) storage conditions. Loyang's products do not show a simple evolutionary sequence from oldest to youngest stratigraphic unit (Figure S2). Rather, the system seems to oscillate between evolved and primitive major element oxide components across the early, middle, and late eruptive stages defined in earlier geological literature (Harijoko, Gunawan, et al. 2018). Among incompatible minor and trace elements like P and Zr, respectively, we see an increase with decreasing MgO or increasing SiO_2, with a minor amount of compositional offset between the two volcanoes (Figures 3d and f).

6.2 Interpreting Olivine Compositions: Mass Balance Models

The whole rock and trace element chemistry of our samples (Figures S2 and 3) point to a simple FC control on the bulk system chemistry. Similar FC controls have been observed in other polygenetic-monogenetic systems (Walowski et al. 2019; Rawson et al. 2016; Larrea et al. 2021). To test if FC can explain the chemical composition of Slamet and Loyang's olivine crystal cargo in greater detail (Figure 5, 7b through f), we designed a mass balance model (discussed in the Methods section) to test which specific FC assemblages could explain Fo vs. Ni systematics in olivine under conditions rhyolite-MELTS struggles to replicate. The Fo vs. Ni trends (Figure 7a) show a concave up pattern, with a wide spread in Ni contents among olivine cores at low Fo - between 50 and 1600 ppm. The primitive olivine (Ol1 and OL2 Figure 9 and 10) trends in Figure 7 are best explained by fractional crystallization from a parental basaltic melt (Figure 7a).

As noted earlier, this family of high-Fo, high-Ni olivine is only found at Loyang (Figure 5, and some of these olivine are associated with the highest entrapment pressures within melt inclusions (Figure S10). Notably, despite each mass balance model having a significantly different FC assemblages, each FC model curve overlaps within error (Figure 7a). Thus, while fractional crystallization is an important control on the most primitive olivine, the mineralogy of the resulting assemblage (and therefore the pressure, temperature, and compositional, or PTX, conditions controlling such fractionation) seems to play a minimal role in driving olivine chemistry. In contrast to these FC trends, some of the olivine cores at Loyang and nearly all the cores of Slamet lie at elevated Ni with respect to expected Fo contents, and these evolved olivine (clusters Ol3 and Ol4, Slamet Type 1 and Loyang Type 1, 4, 5) cannot be adequately explained by fractional crystallization from the same basaltic source liquid as the primitive olivine (Figure 7a and 10a). This high-Ni, low-Fo association typifying the evolved olivine is a common trend among olivine in many magmatic systems, like Kīlauea (Lynn, Shea, and Garcia 2017), Shiveluch (Gordeychik, Churikova, Kronz, et al. 2018; Gordeychik, Churikova, Shea, et al. 2020), Klyuchevskoy and Zarechny (Gordeychik, Churikova, Shea, et al. 2020), and the Central Mexican Volcanic Belt (Straub et al. 2008). In all of these systems, Fo-Ni systematics are explained by magma mixing (Straub et al. 2008; Lynn, Shea, and Garcia 2017), leading to diffusive reequilibration of primitive olivine within a more evolved melt during magma transport (Gordeychik, Churikova, Kronz, et al. 2018; Gordeychik, Churikova, Shea, et al. 2020), or in the case of our Type 4 and 5 olivine, reequiibration with a primitive melt after having crystallized in a more evolved magma. Diffusive reequilibration (as a function of magma mixing) within olivine has been shown to produce "concave down" Ni-Fo trends at moderate-Ni, low-Fo, compared to the "concave up" trends seen in our FC models (Gordeychik, Churikova, Shea, et al. 2020). This concave-down shape derives from the equation used (Gordeychik, Churikova, Shea, et al. 2020) to relate Ni and Fo; the equation in question shares a similar form to Newton's cooling law:

$$\Delta_{\mathrm{Ni}} = (\Delta_{\mathrm{Fo}})^{\frac{\tau_{\mathrm{Fo}}}{\tau_{\mathrm{Ni}}}} \tag{5}$$

where

$$\Delta_C (C being either Ni or Fo) = \frac{C - C_{\mathrm{m}}}{C_0 - C_{\mathrm{m}}} \tag{6}$$

and C_m represents the boundary conditions (i.e. rim composition) and C_0 the initial condition (i.e. core composition); τ_{Fo} and τ_{Ni} are the homogenization times of Fo and Ni respectively, where homogenization times depend on crystal shape, size, and diffusion coefficients (Gordeychik, Churikova, Shea, et al. 2020). Our olivine core compositions, albeit with a wide scatter, fit this concave-down pattern better the further away from the FC curves (Figure 7a). Using theoretical and computational models, olivine of diverse morphologies, geological origin, and chemical composition were used to quantify the relative diffusion time scales of Ni vs. Fe and Mg (Gordeychik, Churikova, Kronz, et al. 2018; Gordeychik, Churikova, Shea, et al. 2020). These models (in 2D and 3D) show that crystal shape and diffusion anisotropy do not significantly modify the diffusion-controlled concave-down trend of elevated Ni with respect to low Fo. Rather, as shown mathematically above, the shape of this trend is mainly driven by the ratio of the Ni vs. Fo diffusion coefficients, and the trend's are controlled by the compositional contrast between the mafic versus the more evolved melts that have mixed to cause the diffusion (Gordeychik, Churikova, Shea, et al. 2020). These models show that Ni diffuses more slowly than Fe and Mg - thus, olivine experiencing disequilibrium will see Fo lowered at a faster rate than Ni (Gordeychik, Churikova, Kronz, et al. 2018; Gordeychik, Churikova, Shea, et al. 2020).

While there are few empirically defined $D_{Ni}^{ol-melt}$ designed for arc systems, if we assumed that at lower temperatures Ni might behave less compatibly, perhaps due to fractionated sulfides which are abundant in all arc magmas (Paul J Wallace and Edmonds 2011; Barber et al. 2021), our FC curves might explain why some of the high-Ni, low-Fo olivine currently best matched by Ni's diffusivity contrast with Fo (Gordeychik, Churikova, Shea, et al. 2020). Addressing this uncertainty will require further empirical work on olivine in hydrous, low-temperature systems.

6.3 Crystal Cargoes Indicate Mush Transport and Storage

Olivine core populations in both Loyang and Slamet samples have core compositions of Fo_{65} to Fo_{85} (see Figure 5 and 7), indicating that some olivines formed under fairly evolved conditions. Forsterite contents $>Fo_{88}$ would be expected for olivine in equilibrium with the mantle (Conway et al. 2020; McGee et al. 2013; Straub et al. 2008). For mantle-derived, primitive olivine, trace element concentrations of Ni (see Figure 8), should lie between 2000 and 5000 ppm (Straub et al. 2008; McGee et al. 2013; Gordeychik, Churikova, Kronz, et al. 2018; Gordeychik, Churikova, Shea, et al. 2020; Lynn, Shea, and Garcia 2017). Instead, our olivines have a maximum Ni of around 1600 ppm, and as shown in Figures 7a; in some crystals the Ni is as low as 200 ppm. These chemical patterns indicate that most of these olivine cores, including all those measured from Slamet and many early stage Loyang olivine, formed in fractionated mantle melts. The ranges in Fo and Ni contents (Fo_{65} to Fo_{85} and 50 to 1600 ppm Ni) are quite low by global standards (Figure 5 and 7). Both Slamet and Loyang whole-rock compositions have Mg#s between 45 and 60 (Figure 7b), again indicating a relatively evolved source melt.

Plotting the Fo content of melt inclusion-host olivine from both Slamet and Loyang against their corresponding melt inclusion glass compositions (Figure 5b) reveals that these olivine mostly are out of equilibrium with associated primitive melt composition, likely captured when the olivine first grew. In general, melt inclusion-hosting olivines are more evolved than their captured melts. Slamet is composed almost exclusively of evolved olivine (Figure 5). Loyang's olivine cores show strong relationships between Fo content and the stratigraphic stage of a given sample (Figure 5). As shown in Figure 5a, from L1 through to L8 (the early to middle stage eruptions (Harijoko, Gunawan, et al. 2018)), olivine Fo content increases. By the mid- (L7 and L8) to late-stage (L10) eruptions, this trend drops off, and olivine appear bimodally distributed with some evolved and some primitive olivine carried during this eruption. These initial observations provide a picture of the primary magmatic system feeding both this polygenetic centre and its flank scoria cone: while most olivine across both centres form in the presence of a primitive melt, some from Loyang and almost all from Slamet derive from a more evolved melt. At Loyang, these evolved olivines most commonly appear in the early and late stage eruptive events (Figure S1), suggesting Loyang is erupting olivine that has crystallized from (1) distinct batches of magma from Slamet, or (2) from the same magma sampled at a later, more fractionated, stage in its history.

As presented schematically in Figure 6, qualitative data in the form of the textural features across Slamet and Loyang olivine also provide evidence of physical mixing between different composition melts, producing variably resorbed and zoned olivine. In zoned olivine, these textural features are defined by BSE grey-scale variations and abundant melt inclusions (Figure 8e-j). Based on these systematic observations across our entire olivine dataset, we have developed a classification scheme for Slamet and Loyang's olivine that shares some similarities with prior classification schemes at Slamet (Reubi, I. A. Nicholls, and Kamenetsky 2003). The difference between our Slamet textural scheme and earlier schemes (Reubi, I. A. Nicholls, and Kamenetsky 2003) is that we define sub populations of unzoned olivine to distinguish between unzoned olivine that is equant and that which is anhedral. Furthermore, we distinguish two modes of reverse zoning - "minor" and "major" depending on the relative Fe difference from core to rim, as well as the presence of widespread melt inclusions marking out major reverse zoned olivine:

- Type 1 olivine (Figure 6a): Homogeneous (i.e. unzoned or "chemically homogeneous") olivine with no evidence of zoning or resorption. Average olivine core compositions of Fo_{80} and 990 ppm Ni.

- Type 2 (Figure 6b): Homogeneous olivine with evidence of resorption (rounded edges or small embayments). Average olivine core compositions of Fo_{80} and 990 ppm Ni, identical to Type 1.
- Type 3 (Figure 6c): Normally-zoned olivine; Type 3 olivine show conspicuously lower Fo% on the rim compared to their core. Average olivine core compositions of Fo_{82} and ∼1000 ppm Ni. Varying degrees of resorption.
- Type 4 (Figure 6d): Minor reverse-zoned olivine. Difference in Fo content between core and rim is the opposite sense of Type 3 olivine; rim has higher Fo% than core. Type 4 olivine have an absolute core-to-rim Fo% difference of <8%. Average olivine core compositions of Fo_{74} and 460 ppm Ni. Varying degrees of resorption, but usually not as resorbed as Type 5.
- Type 5 (Figure 6e): Major reverse zoned olivine. Difference in Fo% contents between core and rim is >8%. Average olivine core compositions of Fo_{67} and 480 ppm Ni. Highly resorbed, with significant evidence of embayment.

These different physiochemical groupings are summarized schematically in Figure 12. As seen in the schematic, homogeneous olivine (Type 1 and 2) from Loyang have much higher Fo content compared to homogeneous olivine in Slamet, consistent with some Loyang magmas (those feeding middle-stage Loyang eruptions, L3—L8) having a source magma made of much more primitive liquid than that forming their Slamet counterparts. Slamet only preserves these hybrid to evolved olivine across all textural types. In contrast, Loyang shows a broad range of primitive, hybrid, and evolved olivine, with the most primitive being from Type 1 and 2, and the most evolved being from Type 4 and 5. Type 3 olivine (primarily at Loyang) show primitive core compositions similar to Type

1 and 2 olivine (Figure 7). However, we argue that during transport these olivine came into contact with a more evolved liquid, leading to their zoning. At the same time, Type 4 and 5 olivine from both systems show evidence of being crystallized in an evolved liquid, before being carried by a more primitive liquid, introducing the reverse zoning seen to a large degree in some Loyang olivine (Figure 8).

The consistency of this overlap indicates a petrogenetic connection between these evolved olivine in both systems. For example, the few evolved Type 1 Loyang olivine almost exclusively group with similar Slamet olivine on Fo vs. Ni plots (Figure 7b). While we can plainly see an absence of primitive olivine at Slamet, the mixture of evolved, hybrid, and primitive olivine present, particularly in Type 1 and Type 5 olivine (Figure 7a&f and 8) at Loyang, point to Loyang magmas interacting with and sometimes capturing material from a reservoir that is shared by Slamet in the upper crust. This interpretation is reinforced by the compositions of both pyroxenes (Figure S4) and feldspars (Figure S5). The Mg# content of pyroxenes decreases with stratigraphy at Loyang (Figure S4) reflecting a hybrid cargo of evolved and primitive crystals being tapped during late stage Loyang eruptions (Figure 5 and S4). Feldspar cores are below An_{80} (between An_{80} and An_{60} at Slamet (Figure S5), consistent with their growth in relatively evolved, intermediate composition melts (Cashman, Sparks, and Blundy 2017). Like our evolved (Ol3 and Ol4) olivine (Figure 7d-f), some pyroxenes and most feldspars are compositionally biased towards a more evolved magmatic origin. We envision a shallow to mid-crustal storage zone dominated by crystals with an interstitial, evolved melt (Cashman, Sparks, and Blundy 2017; Edmonds et al. 2019) (Figure 12).

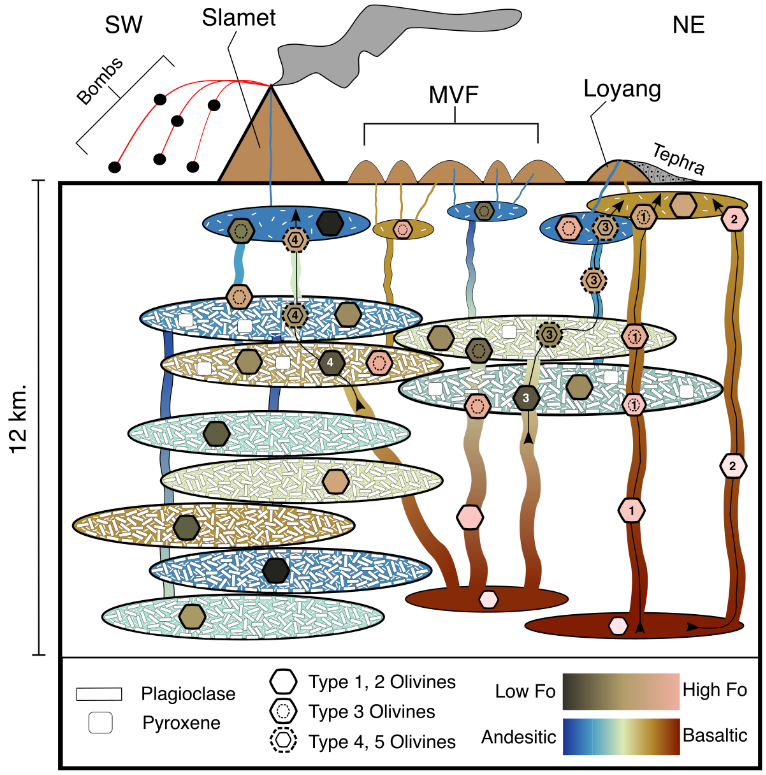

Figure 12: Schematic showing proposed plumbing system feeding Slamet volcano and Loyang monogenetic cone, Java, Indonesia. Sources of different olivine types inferred from Ni, Fo, and melt inclusion trends, plagioclase source from mineral chemistry, and pyroxene sources inferred from mineral chemistry and melt inclusion trends. See text for more details. "Pathways," that explain the textural/chemical associations are modeled in this schematic: (1) a high Fo olivine experiences equilibration with the shallow transcrustal mush as it ascends from a basaltic source magma to erupt at Loyang (Type 3, Ol2 cluster); (2) A primitive olivine passes unmodified through the crystal mush, preserving its chemistry and entrapment pressures (Type 1/2, Ol1 cluster); (3 & 4) AN evolved olivine crystallized in the crystal mush is captured by basaltic intrusions ascending from the source basaltic melts. On ascent, this olivine equilibrates with the more mafic melt, producing a reverse zoned texture (Type4/5, depending on length of time in contact with mafic melt) and an slower Ni diffusion rate relative to Fo, leading to elevated Ni relative to the lower Fo (Ol2/3).

6.4 Comparison of Textural Scheme vs. Clustering

Our classification scheme described above is subjective, with few quantitative metrics (with the exception of the 8 Fo% threshold used to distinguish Type 4 and 5 olivine) separating the different olivine types which lack a clear statistical basis. Additionally, the scheme only harnesses the Ni, Fe, and Mg concentrations of our olivine. Taking these trace elements into account using the Boschetty model (Boschetty et al. 2022) (see Method section for details), we find that identified clusters broadly agree with our existing textural classification scheme. We distinguish four compositional clusters within our olivine (Figure 9), with Ol1 being the most primitive (highest Fo and Ni concentrations, lowest SiO_2, FeO, MnO concentrations) sub-population and Ol4 the most evolved (see Table 3). We also see variability in Loyang's chemistry as a function of stratigraphy in Figure 10, which show the proportion of olivine clusters contained within each textural olivine type.

Just as with our earlier analyses of Fo content systematics (Figure 5), the olivine clusters vary with the stratigraphy at Loyang (Figure 10b. Early stage samples (L1 and L3), while compositionally dominated by olivine classified as mafic (Ol1 and Ol2), still contain significant portions of evolved olivine (Ol3 and Ol4) (Figure 10b. Thus, while middle stage Loyang samples are dominated by primitive olivine sourced from a primitive melt, both the early and late stage eruptions carry a crystal cargo indicative of a hybridized melt source. Slamet's olivine are, by contrast, wholly made up of evolved Ol3 and Ol4 clusters, indicative of this volcano tapping a more evolved, crystal-rich reservoir (Figure 5and 7). Reconciling with the earlier textural classification scheme (section 7, we see that Type 1, 2, and 3 olivine, which are mainly found in Loyang, are made up of the more primitive Ol1 and Ol2 clusters. In contrast, the Type 4 and 5 olivine are made up almost entirely of Ol3 and Ol4 clusters. We posit that the statistical overlap between evolved Loyang and Slamet olivine suggests a common origin for these sub-populations in the upper crust, while the mafic Ol1 and Ol2 Loyang olivine must have equilibrated with a primitive liquid different than that feeding the shared Slamet-Loyang reservoir.

6.5 Storage Depths Indicate Mid-Crustal Storage at Loyang and Slamet

The entrapment pressures of melt inclusions based on their volatile contents span over 4 kbar (12 km) throughout the crust (see Figures 11 and S10). Loyang melt inclusions contain a maximum of 4 wt.% H_2O, indicating that their source magmas are likely water-saturated in upper crustal magma reservoirs. Loyang melts equilibrated across a range of pressures in the mid- to upper crust (at a maximum pressure of 4 kbar or roughly 12 km) (Figures S10 and S11). Slamet melt inclusions, with one exception, almost exclusively have saturation pressures less than 1000 bars (Figure S10), and many show chemical and textural evidence of being extensively degassed (Figure S11c). Clinopyroxene-hosted melt inclusions equilibrated at pressures less than 1000 bars (<3 km.), indicating that most clinopyroxene in these systems forms in shallow crustal reservoirs (Figure 12), though these storage pressures must be regarded as a minimum thanks to the effect of post-entrapment modifications like H^+ diffusion (Hartley et al. 2015). Loyang also shows a stratigraphic evolution with respect to its melt inclusion entrapment pressures (Figure S11), which paints a complex picture of its plumbing system. Early stage (L1) melt inclusions record entrapment pressures similar to Slamet, <1000 bars (Figure S11). This eruptive stage is characterized by a large fraction of evolved olivine (Ol3 and Ol4 clusters, Type 1 and Type 5 groups, Figures 5 and 10b) reminiscent of Slamet's olivine crystal cargo. As Loyang evolves, it continually taps deeper-stored melts, until the late stage

(L10) when it erupts a polybaric assemblage of melt inclusions (Figure S11), including the most volatile-rich melt inclusions hosted in the most primitive crystals (Figure 11).

Slamet, by contrast, shows almost uniformly low volatile concentrations in its melt inclusions (Figure S10), with the exception of S303B's melt inclusion which records the highest CO_2 concentration ($\simeq$ 2300 ppm) and entrapment pressure ($\simeq$ 3800 bars) measured across both Slamet and Loyang. This high CO_2 content originates mostly from the vapor bubble (1800 ppm), whereas the host glass shows much lower CO_2 content (500 ppm). This finding illustrates the importance of measuring vapor bubble CO_2 using techniques like Raman spectroscopy. This melt inclusion's abnormal volatile content indicates that while Slamet melt inclusions generally record, shallow, degassed melts, some Slamet olivine must have formed in reservoirs at depth (Figure 12). However, this high pressure Slamet melt inclusion differs from Loyang melt inclusions in a few key respects. First, unlike several higher CO_2 Loyang melt inclusions, S303B's melt inclusion is hosted in an evolved (Fo_{70}) olivine. This is consistent with the rest of Slamet's mineral chemistry, but indicates that at depth, there may be more evolved melts feeding Slamet's magmatic plumbing system compared to Loyang (Figure 12). Second, S303B's H_2O content is nearly below the detection limit, unlike high CO_2 Loyang melt inclusions which have correspondingly high H_2O concentrations (Figure 11). This inconsistency could be reconciled where Slamet is mainly fed by anhydrous melts, and where hydrous melts are recorded these are originating from the more basaltic system feeding Loyang. The offset between S303B's glass and vapor bubble CO_2 contents, coupled with its relatively low PEC ($<$10%), point to a vapor bubble which formed syn-eruption, while the liquid could diffuse mobile CO_2 into the bubble before eruption (Wieser et al. 2021).

6.6 The Slamet-Loyang Plumbing System

Integrating our observations across both edifices, we envisage a shared Slamet-MVF plumbing system as shown in Figure 12. More Fo-rich olivine crystallises from a basaltic melt at depth, then ascends and passes through a shallow, more evolved reservoir which is primary magmatic source for Slamet and its surrounding MVF, including Loyang. The primitive liquids feeding Loyang's most mafic eruptions must be sourced from mid-crustal (∼12 km or deeper) basaltic melt reservoirs, while the majority of melt inclusions across both volcanoes record shallow crustal (3 km) storage in a largely degassed reservoir (Figure 11). The basaltic melt is not in equilibrium with the mantle, and therefore has been stored in the mid or lower crust at least 12 km below Loyang (Figure 12), where it has fractionated an assemblage of olivine and clinopyroxene phenocrysts. While some primitive olivine transit this upper crust plumbing system unmodified (Ol1 and Ol2 clustered olivine with Type 1 and Type 2 textures), some interact directly with the evolved shallow melt reservoir feeding the Slamet-Loyang magmatic system at shallow levels, leading to chemical and textural zoning (Type 3 olivine).

At both Slamet and Loyang, evolved olivine (Ol3 and Ol4 clusters including all Slamet olivine and some Type 1, 4, and 5 Loyang olivine) crystallized in the shallow crustal reservoir form in a relatively-degassed, compositionally-distinct reservoir from primitive olivine. The evolved reservoir underlying Slamet is likely polybaric, as evidenced by melt inclusions (Figure S11), extending to similar depths as the basaltic melts that in-turn interact with Slamet magmas and feed Loyang's eruptions. At Loyang, evolved olivine are primarily tapped during eruption initiation, and tapped again during the late stage eruptions. All evolved and hybrid olivine remain in contact with the evolved melt, their host melts gradually degas, and the crystals are eventually erupted via Strombolian-style eruptions at Slamet, Loyang, or potentially at other spatially associated MVFs. Some of the evolved olivine (Type 4 and 5) preserve textural evidence of mingling with a basaltic liquid, likely the same composition liquid Loyang is erupted during its mafic eruptive stages.

These zoning patterns require a basaltic liquid to mingle with a more evolved, and likely shallow, crustal reservoir as seen in other MVFs, e.g., the Kaikohe-Bay of islands MVF, NZ (Coote and Shane 2018). This magma mingling process will lower the Fo content of primitive olivine entrained in the melt transport network, while simultaneously picking up evolved olivine from the shallow reservoir and making their rims high in Fo and Ni. Therefore, Loyang, like other monogenetic volcanoes (Romero et al. 2022; Gao, Lassiter, and Ramirez 2017; Jankovics, Sági, et al. 2019; Cameron et al. 2010), shows strong evidence for the open system magmatism, where multiple generations of melt mingle and erupt at one scoria cone over its short lifespan. However, Loyang shows not only a complex petrological history, but parts of that history e.g., the evolved Type 1 and 2 olivine in L1 and L10 show nearly identical chemical and textural overlap with those evolved olivine from Slamet. We argue that it is the mingling process that creates the textual/chemical associations which informed our understanding of this magmatic system as a multi-staged magmatic plumbing system sharing some connectivity between the mafic primary melts the ultimately feed Loyang's late stage eruptions, and the evolved, shallow mush that feeds both Slamet and Loyang's more evolved eruptions(Figure 12).

The bimodal storage depth assemblage among melt inclusions corresponds to a similarly bimodal compositional assemblage of Ol1 vs. Ol4 clusters also observed in L10 (Figure 10a and b). This indicates that, unlike earlier primitive olivine, those sourced from this late stage eruption derive from mid-crustal primitive melts (schematically shown in Figure 12). The Slamet-Loyang magmatic system therefore contains distinct melt reservoirs, with Loyang first tapping shallow melt reservoirs representing a range of chemical compositions (primitive, hybrid, and evolved), and finally tapping the deepest, most mafic, material as it reached the end of its short eruptive period. The earlier hybrid and evolved material at Loyang, trapped at such shallow depths, shares similar entrapment pressure (Figure 11) and host crystal chemistry (Figure 10b and S10b) ranges as those observed in Slamet's melt inclusions. These trends bear some resemblance to those identified at Hauhungatahi (Cameron et al. 2010) and Kaikohe Bay, NZ (Coote and Shane 2018), where distal scoria cones are found to tap increasingly primitive, deeper-sourced material over the course of their eruptions. In this case, this mafic material was brought up through an evolved crystal-rich reservoir, which had earlier supplied most of Loyang's eruptive material (Figure 12).

Both Slamet and Loyang preserve evidence of shallow, heavily degassed reservoirs (see Figure 12) which share some chemical affinity, but Slamet notably lacks the primitive olivine found in Loyang even at mid-crustal depths (Figure 11, S10). While storage timescales in these magma mushes are beyond the scope of this paper, the close temporal association between Loyang and Slamet (roughly Holocene in age (Harijoko, Gunawan, et al. 2018; Agung Harijoko et al. 2021)) indicate that in the MS eruptive period defining modern activity, both Loyang and Slamet shared a shallow crust melt reservoir with distinct surface-level conduits, and in Loyang's case a much more primitive melt source region extending to similar depths as the stratovolcano. We expect similar magmatic architecture underlies the rest of Slamet's MVF, with increasing degrees of contamination from Slamet's evolved transcrustal mush contaminating the primitive, wet source melts of the MVF.

7 Conclusion

In this study we present wide-ranging investigation of the crystal cargo, storage depths, and petrogenesis of the magmas supplying Gunung Slamet, a polygenetic stratovolcano, and Gunung Loyang, one of Slamet's many monogenetic scoria cones a neighboring (14 km distance). Our mineral chemical, and textural results, validated by machine-learning methodologies and enhanced by detailed study of Slamet and Loyang hosted melt inclusions, reveal a three-part magmatic feeder system, with a shallow melt reservoirs feeding each of the eruptive centres (either Slamet and/or one of its scoria cones) (Figure 12). These shallow reservoirs are envisaged as disconnected in the shallow crust, but sharing a deeper (approx. 10 km. depth) common source. Underlying these shallow reservoirs is a laterally and vertically extensive transcrustal mush (Cashman, Sparks, and Blundy 2017). It is is the shallow crust that most plagioclase and clinopyroxene phenocrysts crystallize, and in an evolving, crystal rich environment they develop growth zones and other textural features. Some olivine crystallises in the shallow reservoirs, equilibrated with a more evolved melt, resulting in a lower Fo and Ni content. This evolved olivine is captured by ascending melts and erupted at both Slamet and Loyang. In the deepest parts of this feeder system, olivine with an Fo >75 crystallises. These, more primitive, basaltic melts are tapped to variable degrees by Loyang, which shows textural, chemical, and volatile evidence for a complex crystal cargo. In contrast, Slamet does not show evidence in its olivine crystal cargo of more mafic sources for its olivines.

The depths associated with these saturation pressures (0–12 km) are consistent with an extensive, crystal dominated magmatic mush in the mid-crust, as has been observed at many other arc volcanoes (Cashman, Sparks, and Blundy 2017). Loyang displays a stratigraphic evolution in its olivine compositions, following a "sawtooth" increase, followed by a decrease in primitive basaltic contributions as it evolves from Early—Middle and then Middle—Late stage eruptive products. This evolutionary pattern is found at other compositionally complex monogenetic volcanoes, however, few others display strong textural and compositional evidence of a shared evolved magma reservoir connecting both a polygenetic volcano and its associated MVF. Given that Loyang is one of Slamets most distal scoria cones, it is likely that more proximal scoria cones are also supplied by the same shallow crustal mush feeding both Slamet and Loyangs, as shown by their crystal cargoe's evolved olivine. The shallow portions of this magmatic system show extensive degassing and volatile-loss, explaining why Slamet sees so few large, Vulcanican or larger eruptions compared to its neighbors such as Merapi. This study provides strong motivation for future work in integrated assessments of stratovolcanoes and their associated MVFs to better understand the eruptive history and future magmatic activity at hybrid polygenetic-monogenetic volcanoes.

Data Availability

All of our data, code, and protocols are available at the corresponding author's figshare page. Reviewer's and editors are asked to use this private link to view all supporting code and data. DO NOT SHARE THIS LINK: https://figshare.com/s/dcb3f4bc7429312cf402 The code and figures will be updated in future versions of the database, but all the material pertaining to this paper will be preserved.

Acknowledgements

We would like to thank Paul Antoshechkin (CalTech) for helpful discussions and sharing of MELTS related examples to aid our PEC efforts with clinopyroxene. NDB and ME acknowledge funding from the NERC Centre for the Observation and Modelling of Earthquakes, Volcanoes and Tectonics (COMET). NDB acknowledges this work was supported, in whole or in part, by both the Bill & Melinda Gates Foundation (Grant Number OPP1144) and the Gates Cambridge Trust. We acknowledge further support from NERC to use the Ion-probe facility in Edinburgh (grant no. IMF705/0520). SLB is funded by the Scottish Alliance For Geoscience Environment and Society at the University of Edinburgh. FOB is funded by the NERC Panorama Doctoral Training Partnership (DTP) NE/S007458/1.

CRediT Statement

NDB: Conceptualization, Methodology, Software, Investigation, Formal Analysis, Writing (Original, Review and Edits), Visualization Preparation, Project Management, Data Curation Management. **SLB**: Methodology, Investigation, Formal Analysis, Writing- Original draft preparation. **ME**: Conceptualization, Supervision, Funding Acquisition, Writing - Review & Editing. **FOB**: Software, Validation, Writing - Review & Editing: **HEW**: Sample provision, Investigation: **AH**: Sample provision, Investigation.

Competing Interests

We declare no competing interests.

Materials and Correspondence

All correspondence should be directed to Nicholas D. Barber (nbarber@wlu.edu).

References

Barber, Nicholas D et al. (2021). "Amphibole control on copper systematics in arcs: Insights from the analysis of global datasets". In: *Geochimica et Cosmochimica Acta* 307, pp. 192–211.

Bas, MJ LE et al. (1986). "A chemical classification of volcanic rocks based on the total alkali-silica diagram". In: *Journal of petrology* 27.3, pp. 745–750.

Beattie, Paul, Clifford Ford, and Douglas Russell (Dec. 1991). "Partition coefficients for olivine-melt and orthopyroxene-melt system". In: *Beiträage zur Mineralogie und Petrographie* 109, pp. 212–224.

Boschetty, Felix O et al. (2022). "Insights into magma storage beneath a frequently erupting arc volcano (Villarrica, Chile) from unsupervised machine learning analysis of mineral compositions". In: *Geochemistry, Geophysics, Geosystems* 23.4, e2022GC010333.

Boyce, Julie A et al. (2015). "Variation in parental magmas of Mt Rouse, a complex polymagmatic monogenetic volcano in the basaltic intraplate Newer Volcanics Province, southeast Australia". In: *Contributions to Mineralogy and Petrology* 169.2, p. 11.

Brož, Petr and Ernst Hauber (2012). "A unique volcanic field in Tharsis, Mars: Pyroclastic cones as evidence for explosive eruptions". In: *Icarus* 218.1, pp. 88–99.

Cameron, Errol et al. (2010). "The petrology, geochronology and geochemistry of Hauhungatahi volcano, SW Taupo Volcanic Zone". In: *Journal of Volcanology and Geothermal Research* 190.1-2, pp. 179–191.

Cañon-Tapia, Edgardo (2016). "Reappraisal of the significance of volcanic fields". In: *Journal of volcanology and Geothermal Research* 310, pp. 26–38.

Carn, SA and DM Pyle (2001). “Petrology and geochemistry of the Lamongan Volcanic Field, East Java, Indonesia: primitive Sunda Arc magmas in an extensional tectonic setting?” In: *Journal of Petrology* 42.9, pp. 1643–1683.

Cashman, Katharine V, R Stephen J Sparks, and Jonathan D Blundy (2017). “Vertically extensive and unstable magmatic systems: a unified view of igneous processes”. In: *Science* 355.6331, eaag3055.

Conway, Chris E et al. (2020). “Rapid assembly of high-Mg andesites and dacites by magma mixing at a continental arc stratovolcano”. In: *Geology* 48.10, pp. 1033–1037.

Coote, Alisha and Phil Shane (2018). “Open-system magmatic behaviour beneath monogenetic volcanoes revealed by the geochemistry, texture and thermobarometry of clinopyroxene, Kaikohe-Bay of Islands volcanic field (New Zealand)”. In: *Journal of Volcanology and Geothermal Research* 368, pp. 51–62.

Coote, Alisha, Phil Shane, and Bin Fu (June 2019). “Olivine phenocryst origins and mantle magma sources for monogenetic basalt volcanoes in northern New Zealand from textural, geochemical and Δ18 O isotope data”. In: *Lithos* 344-345.

Crameri, Fabio (May 2019). *Scientific Colour Maps.* Version 5.0.0. The development of the scientific colour maps is supported by the Research Council of Norway through its Centers of Excellence funding scheme, Project Number 223272. DOI: `10.5281/zenodo.3596401`. URL: `https://doi.org/10.5281/zenodo.3596401`.

Edmonds, Marie et al. (Feb. 2019). “Architecture and dynamics of magma reservoirs”. In: *Philosophical Transactions of the Royal Society A: Mathematical, Physical and Engineering Sciences* 377, p. 20180298.

Fermi, Enrico (1931). “Über den ramaneffekt des kohlendioxyds”. In: *Zeitschrift für Physik* 71.3, pp. 250–259.

Gao, Ruohan, John C Lassiter, and Gabrielle Ramirez (2017). “Origin of temporal compositional trends in monogenetic vent eruptions: Insights from the crystal cargo in the Papoose Canyon sequence, Big Pine Volcanic Field, CA”. In: *Earth and Planetary Science Letters* 457, pp. 227–237.

Gencalioglu-Kuscu, Gonca (2011). “Geochemical characterization of a Quaternary monogenetic volcano in Erciyes volcanic complex: Cora Maar (Central Anatolian volcanic province, Turkey)”. In: *International Journal of Earth Sciences* 100.8, pp. 1967–1985.

Ghiorso, Mark and Guilherme Gualda (June 2015). “An H2O–CO2 mixed fluid saturation model compatible with rhyolite-MELTS”. In: *Contributions to Mineralogy and Petrology* 169.

Gordeychik, Boris, Tatiana Churikova, Andreas Kronz, et al. (2018). “Growth of, and diffusion in, olivine in ultra-fast ascending basalt magmas from Shiveluch volcano”. In: *Scientific Reports* 8.1, pp. 1–15.

Gordeychik, Boris, Tatiana Churikova, Thomas Shea, et al. (2020). “Fo and Ni Relations in Olivine Differentiate between Crystallization and Diffusion Trends”. In: *Journal of Petrology* 61.9, egaa083.

Gualda, Guilherme AR et al. (2012). “Rhyolite-MELTS: a modified calibration of MELTS optimized for silica-rich, fluid-bearing magmatic systems”. In: *Journal of Petrology* 53.5, pp. 875–890.

Hackett, WR and BF Houghton (1989). “A facies model for a Quaternary andesitic composite volcano: Ruapehu, New Zealand”. In: *Bulletin of volcanology* 51.1, pp. 51–68.

Harijoko, A, RMPP Gunawan, et al. (2018). “Formation of Mount Loyang: Easternmost Scoria Cone of Slamet Stratovolcano, Central Java, Indonesia”. In: *AIP Conference Proceedings* 1987, p. 020063.

Harijoko, A, AN Milla, et al. (2020). “Magma evolution of Slamet Volcano, Central Java, Indonesia based on lava characteristic”. In: *IOP Conference Series: Earth and Environmental Science*. Vol. 451. IOP Publishing, p. 012092.

Harijoko, A, RA Noor, et al. (2018). “Petrological and geochemical characteristics of pumiceous tephra deposit from Slamet stratovolcano, Central Java, Indonesia: Explosive period of the most differentiated magma of a basaltic stratovolcano”. In: *AIP Conference Proceedings*. Vol. 1987. AIP Publishing LLC, p. 020060.

Harijoko, Agung et al. (2021). “Stratigraphy, chronology, and magma evolution of Holocene volcanic products from Mt. Slamet deposited in the Guci Valley, Central Java, Indonesia”. In: *Journal of Volcanology and Geothermal Research* 418, p. 107341.

Hartley, Margaret E et al. (2015). “Diffusive over-hydration of olivine-hosted melt inclusions”. In: *Earth and Planetary Science Letters* 425, pp. 168–178.

Houghton, BF and WR Hackett (1984). “Strombolian and phreatomagmatic deposits of Ohakune Craters, Ruapehu, New Zealand: a complex interaction between external water and rising basaltic magma”. In: *Journal of volcanology and geothermal research* 21.3-4, pp. 207–231.

Iacovino, Kayla, Meghan R Guild, and Christy B Till (2020). “Aqueous fluids are effective oxidizing agents of the mantle in subduction zones.” In: *Contributions to Mineralogy & Petrology* 175.4.

Iacovino, Kayla, Simon Matthews, et al. (2021). “VESIcal Part I: An open-source thermodynamic model engine for mixed volatile (H2O-CO2) solubility in silicate melts”. In: *Earth and Space Science* 8.11, e2020EA001584.

Ivanov, Mikhail A and James W Head (2013). “The history of volcanism on Venus”. In: *Planetary and Space Science* 84, pp. 66–92.

Jankovics, M Éva, Szabolcs Harangi, et al. (2015). “A complex magmatic system beneath the Kissomlyó monogenetic volcano (western Pannonian Basin): evidence from mineral textures, zoning and chemistry”. In: *Journal of Volcanology and Geothermal Research* 301, pp. 38–55.

Jankovics, M Éva, Tamás Sági, et al. (2019). “Olivine major and trace element compositions coupled with spinel chemistry to unravel the magmatic systems feeding monogenetic basaltic volcanoes”. In: *Journal of Volcanology and Geothermal Research* 369, pp. 203–223.

Johnson, Emily R and Katharine V Cashman (2020). “Understanding the storage conditions and fluctuating eruption style of a young monogenetic volcano: Blue Lake crater ($<$ 3 ka), High Cascades, Oregon”. In: *Journal of Volcanology and Geothermal Research* 408, p. 107103.

Kereszturi, Gábor and Károly Németh (2012). “Monogenetic basaltic volcanoes: genetic classification, growth, geomorphology and degradation”. In: *Updates in volcanology-new advances in understanding volcanic systems*. IntechOpen.

Lamadrid, HM et al. (2017). “Reassessment of the Raman CO2 densimeter”. In: *Chemical Geology* 450, pp. 210–222.

Larrea, Patricia et al. (2021). “From explosive vent opening to effusive outpouring: mineral constraints on magma dynamics and timescales at Paricutin monogenetic volcano”. In: *Journal of Petrology* 62.4, egaa112.

Li, Chusi and Edward M Ripley (2010). “The relative effects of composition and temperature on olivine-liquid Ni partitioning: Statistical deconvolution and implications for petrologic modeling”. In: *Chemical Geology* 275.1-2, pp. 99–104.

Lynn, Kendra J, Thomas Shea, and Michael O Garcia (2017). “Nickel variability in Hawaiian olivine: Evaluating the relative contributions from mantle and crustal processes”. In: *American Mineralogist* 102.3, pp. 507–518.

Marliyani, Gayatri Indah et al. (2020). “Volcano morphology as an indicator of stress orientation in the Java Volcanic Arc, Indonesia”. In: *Journal of Volcanology and Geothermal Research* 400, p. 106912.

McGee, Lucy E et al. (2013). “Asthenospheric control of melting processes in a monogenetic basaltic system: a case study of the Auckland Volcanic Field, New Zealand”. In: *Journal of Petrology* 54.10, pp. 2125–2153.

Németh, K and G Kereszturi (2015). “Monogenetic volcanism: personal views and discussion”. In: *International Journal of Earth Sciences* 104.8, pp. 2131–2146.

Philibosian, Belle and Mark Simons (Nov. 2011). “A survey of volcanic deformation on Java using ALOS PALSAR interferometric time series”. In: *Geochemistry, Geophysics, Geosystems* 12.11. ISSN: 1525-2027. DOI: `10.1029/2011GC003775`. URL: `https://doi.org/10.1029/2011GC003775`.

Rasmussen, Daniel J et al. (2020). “Vapor-bubble growth in olivine-hosted melt inclusions”. In: *American Mineralogist* 105.12, pp. 1898–1919.

Rawson, Harriet et al. (2016). “Compositional variability in mafic arc magmas over short spatial and temporal scales: evidence for the signature of mantle reactive melt channels”. In: *Earth and Planetary Science Letters* 456, pp. 66–77.

Reubi, Olivier, Ian A Nicholls, and Vadim S Kamenetsky (2003). “Early mixing and mingling in the evolution of basaltic magmas: evidence from phenocryst assemblages, Slamet Volcano, Java, Indonesia”. In: *Journal of Volcanology and Geothermal Research* 119.1-4, pp. 255–274.

Roeder, P L and R F l Emslie (1970). “Olivine-liquid equilibrium”. In: *Contributions to mineralogy and petrology* 29.4, pp. 275–289.

Romero, Jorge E et al. (2022). “The eruptive history and magma composition of Pleistocene Cerro Negro volcano (Northern Chile): Implications for the complex evolution of large monogenetic volcanoes”. In: *Journal of Volcanology and Geothermal Research*, p. 107618.

Rose-Koga, EF et al. (2021). “Silicate melt inclusions in the new millennium: A review of recommended practices for preparation, analysis, and data presentation”. In: *Chemical Geology*, p. 120145.

Smith, Ian EM, Marco Brenna, and Shane J Cronin (2021). “The magma source of small-scale intraplate monogenetic volcanic systems in northern New Zealand”. In: *Journal of Volcanology and Geothermal Research* 418, p. 107326.

Smith, IEM and K Németh (2017). “Source to surface model of monogenetic volcanism: a critical review”. In: *Geological Society, London, Special Publications* 446.1, pp. 1–28.

Straub, Susanne M et al. (2008). “Evidence from high-Ni olivines for a hybridized peridotite/pyroxenite source for orogenic andesites from the central Mexican Volcanic Belt”. In: *Geochemistry, Geophysics, Geosystems* 9.3.

Sutawidjaja, Igan S and R Sukhyar (2009). “Cinder cones of Mount Slamet, Central Java, Indonesia”. In: *Indonesian Journal on Geoscience* 4.1, pp. 57–75.

Sutawidjaja, IS, D Aswin, and K Sitorus (1985). “Geologic map of Slamet Volcano, Central Java, scale 1: 50.000”. In: *Volcanological Survey of Indonesia.*

Valentine, GA and TKP Gregg (2008). “Continental basaltic volcanoes—processes and problems”. In: *Journal of Volcanology and Geothermal Research* 177.4, pp. 857–873.

Venzke, E (2013). "Global volcanism program". In: *Volcanoes of the World* 4, p. 4.

Vigouroux, Nathalie et al. (Sept. 2012). "The sources of volatile and fluid-mobile elements in the Sunda arc: A melt inclusion study from Kawah Ijen and Tambora volcanoes, Indonesia". In: *Geochemistry, Geophysics, Geosystems* 13.9. ISSN: 1525-2027. DOI: 10.1029/2012GC004192. URL: https://doi.org/10.1029/2012GC004192.

Vukadinovic, Danilo and Ian Nicholls (Sept. 1989). "The petrogenesis of island arc basalts from Gunung Slamet volcano, Indonesia: Trace element and 87Sr /86Sr constraints". In: *Geochimica et Cosmochimica Acta* 53, pp. 2349–2363.

Vukadinovic, Danilo and Igan Sutawidjaja (1995). "Geology, mineralogy and magma evolution of Gunung Slamet volcano, Java, Indonesia". In: *Journal of Southeast Asian Earth Sciences* 11.2, pp. 135–164.

Walker, George PL (1993). "Basaltic-volcano systems". In: *Geological Society, London, Special Publications* 76.1, pp. 3–38.

Wallace, Paul J and Marie Edmonds (2011). "The sulfur budget in magmas: evidence from melt inclusions, submarine glasses, and volcanic gas emissions". In: *Reviews in Mineralogy and Geochemistry* 73.1, pp. 215–246.

Walowski, Kristina J et al. (2019). "Understanding melt evolution and eruption dynamics of the 1666 CE eruption of Cinder Cone, Lassen Volcanic National Park, California: insights from olivine-hosted melt inclusions". In: *Journal of Volcanology and Geothermal Research* 387, p. 106665.

Wheller, G E et al. (1987). "Geochemistry of quaternary volcanism in the Sunda-Banda arc, Indonesia, and three-component genesis of island-arc basaltic magmas". In: *Journal of Volcanology and Geothermal Research* 32.1, pp. 137–160. ISSN: 0377-0273. DOI: https://doi.org/10.1016/0377-0273(87)

90041-2. URL: http://www.sciencedirect.com/science/article/pii/0377027387900412.

Widiyantoro, Sri and Rob van der Hilst (1997). "Mantle structure beneath Indonesia inferred from high-resolution tomographic imaging". In: *Geophysical Journal International* 130.1, pp. 167–182.

Wieser, PE et al. (2021). "Reconstructing magma storage depths for the 2018 Kilauean eruption from melt inclusion CO2 contents: the importance of vapor bubbles". In: *Geochemistry, Geophysics, Geosystems* 22.2, e2020GC009364.

Wood, Charles A (1980). "Morphometric analysis of cinder cone degradation". In: *Journal of Volcanology and Geothermal Research* 8.2-4, pp. 137–160.